Chapter 4

ULTIMATE BEARING CAPACITY OF RING FOOTING RESTED ON TWO-LAYERED SOILS

4.1 INTRODUCTION

The previous chapter has a dual impact: (a) presenting the interior point method-based LB-FELA technique after adequately smoothening the considered yield criterion, and (b) analyzing the bearing capacity of the pile footing embedded into clayey soil with the help of the presented lower bound method. In the present chapter, the axisymmetric LB-FELA technique is implemented to study the bearing capacity of ring foundations rested on two layered soils. The ring footings are commonly used for supporting off-shore and on-shore axisymmetric structures like chimneys, transmission towers, bridges and storage towers. These superstructures are subjected to various dynamic and lateral loading which, in turn, transfers heavy load to the underlying foundation. The ring footing can support heavy loads and also reduces the utilization of construction materials and the associated cost. Therefore, predicting the ultimate bearing capacity of ring footing is quite important in geotechnical engineering.

For the past few decades, a good number of laboratory experiments (Al-Sanad et al., 1993; Ismael, 1996; Ohri et al., 1997; Clark, 1998; Boushehrian and Hataf, 2003; Hataf and Razavi, 2003; and Saran et al., 2003), as well as analytical (Fischer, 1957; Egorov, 1958, 1965; Kumar and Ghosh, 2005; Keshavarz and Kumar, 2017; Gholami and Hosseininia, 2017), and numerical studies (Milovic, 1973; Zhao and Wang, 2008; Benmebarek et al., 2012, 2017; Remadna et al., 2017; Kumar and Chakraborty, 2015; Birid and Choudhaury, 2021; Chavda and Dodagoudar, 2019, 2021; and Keawsawarvong and Lai, 2021) were conducted to understand the collapse behaviour of

ring footing placed on completely homogenous soils. By performing load test experiments, few researchers (Saha, 1978; Al-Sanad et al., 1993; Ismael, 1996; Ohri et al., 1997; Clark, 1998; Boushehrian and Hataf, 2003; Hataf and Razavi, 2003; Saran et al., 2003) investigated the effect of annular geometry, soil parameters, embedment depth, loading characteristics on the bearing capacity of ring foundation. Fishers (1957) and Egorov (1958, 1965) provided an analytical solution for a flexible and rigid ring footing on semi-infinite elastic medium. Kumar and Ghosh (2005), Keshavarz and Kumar (2017), and Gholami and Hosseininia (2017) used method of stress characteristics to investigate the effect of footing roughness, soil friction angle, and r_i/r_0 ratio on bearing capacity factors of ring footing. By using displacement based finite element method, Milovic (1973) determined the stresses and displacement beneath the ring foundation. Zhao and Wang (2008), Benmebarek et al. (2012, 2017), and Remadna et al. (2017) adopted finite-difference code, FLAC, to evaluate bearing capacity factors (N_c, N_q, and N_γ) for ring footing. By employing the lower and upper bound theorems of finite element limit analysis, Kumar and Chakraborty (2015) studied the ultimate bearing capacity factors of ring footing. Most of these studies were conducted on ring footing overlying on single layer of either clay or sand.

A few numerical studies were also conducted to determine the bearing capacity of ring footing placed over different two-layered soils, namely, clays over sand (Moayed et al., 2012; and Saifi et al., 2015), sand layer underlying another sand layer (Das et al., 2021; Khatri et al., 2020), sand layer overlaying a clay layer (Al-Khaddar and Al-Kubaisi, 2015; Yang et al., 2020), and two-layered clays having different strengths (Lee et al., 2016). Moayed et al. (2012) used a finite element-based software ABAQUS and Saifi et al. (2015) used finite difference code, FLAC, to study bearing capacity of ring footing on two-layered soil; where, the upper layer is soft clay and the

underneath layer is a cohesionless sand. They concluded that the bearing capacity decreases with increase in clay layer thickness and radius ratio (r_i/r_0). Al-Khaddar and Al-Kubaisi (2015) considered sandy layer over clayey layer and studied vertical and horizontal stresses at different point affected by inclination of load on ring footing with the usage of PLAXIS. Naseri and Hosseininia (2015) adopted finite difference method to study the impact of non-homogeneity, embedment and rigidity of ring footing placed over elastic finite layer. Dhatrak and Mishra (2016) and Lee et al. (2016) used PLAXIS software to simulate multi layered soil and studied the load carrying capacity of ring footing with respect to radius ratio (r_i/r_0). Dhatrak and Mishra (2016) considered three layered soil reinforced with geogrid whereas Lee et al. (2016) simulated two layered clayey soil with different strength values. Das et al. (2021), Yang et al. (2020), and Khatri et al. (2020) used FELA based software, Optum G2, to study the behavior of ring footing resting on three different combinations of two layered soil, namely, weak sand over strong sand, sand deposits overlying clayey layer, and dense sand underlain by a loose sand layer.

Nevertheless, no rigorous work seems to exist for determining the bearing capacity of ring foundations lying over fully cohesive strata, with an overlaying sand layer, duly considering the effect of surcharge loading and footing roughness. In the present study, an attempt has been made to evaluate the bearing capacity of ring footing on sandy soil lying over clayey soil by using the axisymmetric lower bound limit analysis with finite elements and nonlinear optimization. The effect of surcharge pressure is duly investigated by varying the sandy layer thickness, radius ratio (r_i/r_0), and strength of both the layers.

4.2 PROBLEM STATEMENT AND DOMAIN

A rigid ring footing, as shown in Figure 4.1, with external radius, r_0, and internal radius, r_i, is placed over a sand layer which lies over clayey strata. The top sandy layer is considered to be completely drained and the bottom clayey stratum is considered to be completely saturated and undrained (i.e. $\phi_u = 0°$). Obeying Equation (3.31), the undrained shear strength of the bottom clay varies as below:

$$c_u(z) = c_{u0} + mc_{u0}\frac{(|z| - h)}{r_0} \tag{4.1}$$

where, c_{u0} is the undrained cohesion value at the sand-clay interface and h is the upper layer thickness. Both the soil layers are considered to have the same unit weight and dictated by the perfectly plastic condition and associated flow rule. The ground surface is considered to be horizontal and is subjected to surcharge pressure, q.

The average collapse pressure (p_u) on ring footing can be predicted from the following generalized bearing capacity formula:

$$p_u = \frac{Q_u}{\pi(r_0^2 - r_i^2)} = cN_c + qN_q + \gamma(r_0 - r_i)N_\gamma \tag{4.2}$$

where, (i) Q_u is the magnitude of the vertical collapse load; (ii) N_c, N_q, and N_γ represent the bearing capacity factors of ring footings, due to the components of soil cohesion (c), ground surcharge pressure (q) and soil unit weight (γ), respectively.

Owing to the fact, that the geometrical configuration, material properties, loading conditions, and boundary constraints remain to be symmetric about the axis of the footing and independent of circumferential direction, θ, a planar domain in r-z plane is employed by keeping the axis of the symmetry as one of its vertical boundaries. The radial and the vertical extent are chosen large enough such that the failure zones are well contained within the domain boundaries and the solutions are not affected by any

further extension of the domain. It is noteworthy, that with the increase of sand friction angle the volume of collapse zone increases and hence, the size of the domain is also extended accordingly.

Considering these criteria, the radial and the vertical extent are chosen within $5r_0$ to $20r_0$ and $4r_0$ to $15r_0$ depending on the drained friction angle of sand. The imposed stress boundary conditions are as follows: (i) along the axis of symmetry (AB): $\tau_{rz} = 0$, (ii) along the ground surfaces (AF and ED): $\tau_{rz} = 0$ and $\sigma_z = -q$, and (iii) along the soil-footing interface (EF): $|\tau_{rz}| \leq (c\cot\phi - \sigma_z)\tan\delta$; where δ is the interface friction angle between the footing base and the soil mass. The value of δ is varied between 0 (perfectly smooth) and ϕ (perfectly rough). The considered symmetrical plane of domain and the associated stress boundary conditions are depicted in Figure 4.1. Figure 4.2 illustrates the mesh used in the analysis for $\phi = 35°$ and $c_u/(\gamma r_0) = 0.5$.

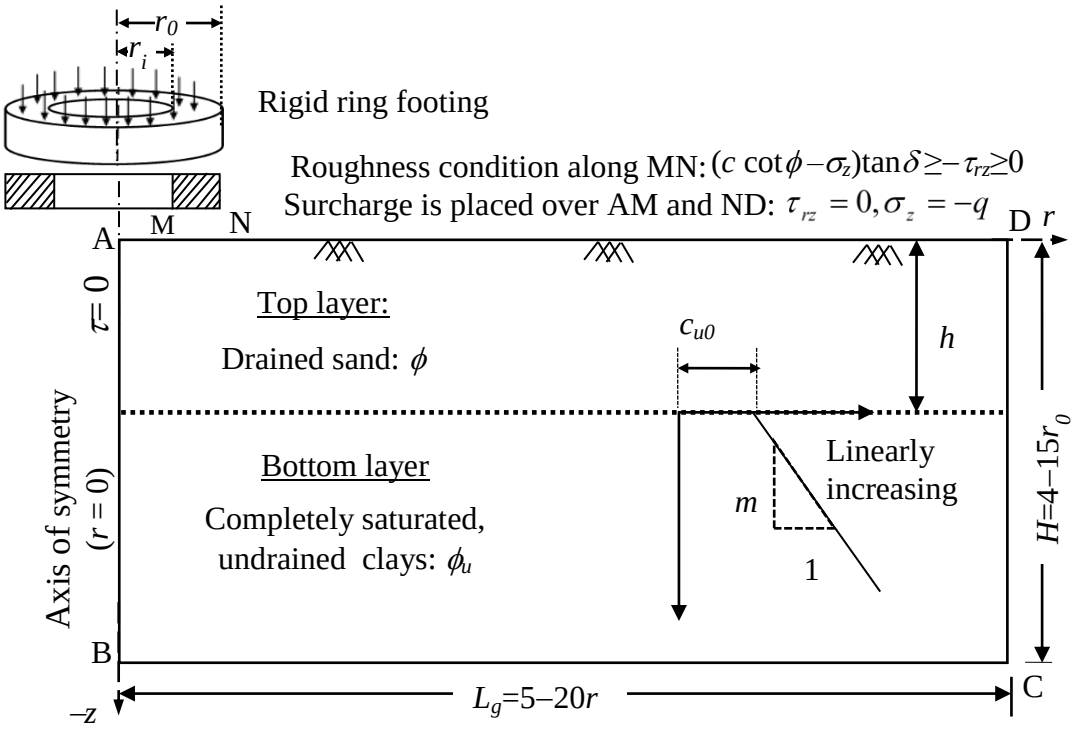

Figure 4.1 Chosen domain and the stress boundary conditions for ring footing on sandy-clay layered medium and cohesion increment in the bottom layer.

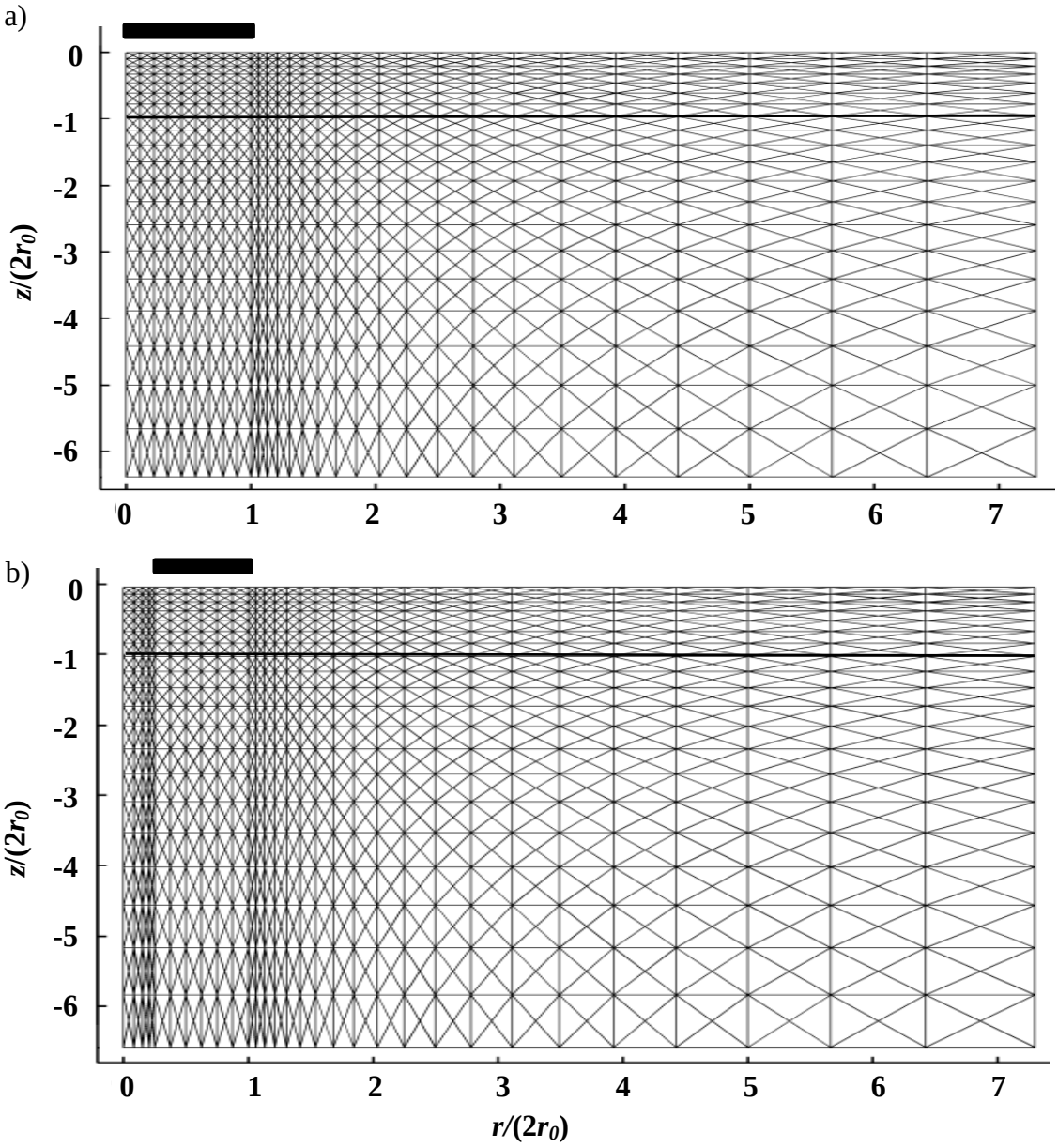

Figure 4.2 Finite element mesh for ϕ = 35° and $c_u/(\gamma r_0)$ = 0.5 with a) h/r_0 = 1, r_i/r_0 = 0; b) h/r_0 = 2, r_i/r_0 = 0.25.

The improvement of the bearing capacity upon the inclusion of sand layer between the ring footing and clayey layer is investigated rigorously for different soil footing interface and surcharge pressure, corresponding to different (i) radius ratio (r_i/r_0 = 0, 0.25, 0.50 and 0.75), (ii) sand friction angle (ϕ = 30°, 35°, 40°, and 45°), (iii) undrained strength of clays ($c_u/(\gamma r_0)$ = 0.1, 0.25, 0.5, 1, 2, 5, 10), (iv) linear rate of cohesion increment (m = 0, 2, and 5), and (v) surcharge pressure ($q/(\gamma r_0)$ = 0, 0.5, and

1). The thickness of the sand layer is varied in wider range (h/r_0 = 0.1 – 10) for all the cases.

4.3 ANALYSIS

To compute the magnitude of p_u, the LB-FELA technique is applied precisely as outlined in the previous chapter (Section 3.2). The smoothened Mohr-Coulomb yield criterion models the top sand (drained) layer and the smoothened Tresca criterion (mentioned in Section 3.2.9) characterizes the bottom clay (undrained) layer. The stress-equilibrium, stress-discontinuity, and stress-boundary conditions generate the equality constraints, whereas, the inequality constraints originate from the soil-footing interface, and the considered yield criterion. After constructing the global equality and non-equality constraints, the total collapse load (objective function) is found by integrating the vertical normal stresses (σ_n) along the footing surface. The problem can be finally expressed into the following non-linear constrained optimization form:

$$\textit{Maximize} \quad Q = 2\pi \int_{r_i}^{r_o} \sigma_n r ds = \boldsymbol{b}^T \boldsymbol{\sigma} \tag{4.3a}$$

$$\textit{Subjected to}: \quad \boldsymbol{A}_{eq}\boldsymbol{\sigma} = \boldsymbol{B}_{eq} \quad \text{and} \quad g(\boldsymbol{\sigma}) \leq 0 \tag{4.3b}$$

The constraint functions are elaborately described in Section 3.2.8 and are not repeated here. By writing suitable code in MATLAB, the IPM based optimization process is carried out to find out the incipient collapse state.

4.4 RESULTS AND DISCUSSION

The improvement of bearing capacity by the inclusion of sand layer is reported by using a non-dimensional efficiency factor (η); where, η is defined as the ratio of bearing capacity of ring footing in presence of sand layer to the bearing capacity of ring

footing placed only over clayey strata. The bearing capacity of the sand-clay layered system can be obtained by multiplying η with the corresponding bearing capacity values presented in Table 4.1. The bearing capacities in this table are reported for different radius ratios, surcharge pressure, undrained cohesive strength, and strength increment rate. It is to be noted that the bearing capacity decreases with an increase in radii ratio.

Figures 4.3–4.6 show the variation of η for homogenous clays corresponding to different values of $c_u/(\gamma r_0)$, ϕ, δ, $q/(\gamma r_0)$ and r_i/r_0. The graphs are plotted for homogenous clays considering perfectly smooth (i.e. $\delta = 0°$) and perfectly rough (i.e. $\delta = \phi$) interface conditions. Figures 4.7–4.10 show the variation of η for non-homogenous clays; Figures 4.7–4.8 are associated with $m = 2$, whereas, Figures 4.9–4.10 correspond to $m = 5$. The observations are listed as follows:

a) It appears that placing the sand beneath the rough ring footing is highly beneficial than its smooth counterpart. This difference of the η value between the smooth and the rough footings reduces with the narrowing of the annular section and the increment of the surcharge pressure adjacent to the footing.

b) It is also noted that insertion of even a thin layer of sand between the footing and the weak clays ($c_u/(\gamma r_0) = 0.1$) enhances the load carrying capacity manifold. The benefits are much more prominent for perfectly rough ring footing having lower values of r_i/r_0 and with the presence of surcharging.

c) On the contrary, the inclusion of sands between ring footing and strong clays ($c_u/(\gamma r_0) = 10$) reduces the bearing capacity of ring footings, especially for the perfectly smooth interfaces. In this context, it is to be noted that clay layers are exclusively characterized by undrained cohesion; the adopted analysis does not incorporate stiffness, density state, or stress history of the soil. Therefore, in

Table 4.1. The ultimate bearing capacity of ring footing placed on homogenous clays for different combination of r_i/r_0, m, and $q/(\gamma r_0)$.

$q/(\gamma r_0)$	r_i/r_0	$c_u/(\gamma r_0)$ =																				
		0.1			0.25			0.5			1			2			5			10		
		m =																				
0	0	0	2	5	0	2	5	0	2	5	0	2	5	0	2	5	0	2	5	0	2	5
	0.25	0.6	2.1	3.5	1.5	2.1	5.1	3	5.2	7.3	6	8.6	11.2	12	15.1	18.2	30.1	33.5	37.7	60.2	63.8	68.8
	0.5	0.6	1.6	2.5	1.5	1.6	3.9	2.9	4.5	5.9	5.9	7.7	9.5	11.7	13.8	16.1	29.3	31.7	34.6	58.6	61.1	64.4
	0.75	0.6	1.3	2	1.4	1.3	3.2	2.8	3.9	5	5.5	6.9	8.26	11.1	12.6	14.3	27.7	29.3	31.4	55.3	56.9	59.4
0.5	0	0.5	1	1.4	1.3	1	2.5	2.6	3.3	4	5.3	6.1	6.96	10.6	11.5	12.5	26.5	27.4	28.6	52.9	53.8	55.2
	0.25	1.1	2.6	4	2	2.6	5.6	3.5	5.7	7.8	6.5	9.1	11.7	12.5	15.6	18.7	30.6	34.1	38.2	60.7	64.3	69.2
	0.5	1.1	2.1	3	2	2.1	4.4	3.4	5	6.4	6.4	8.2	10	12.2	14.3	16.6	29.8	32.1	35.1	59.1	61.3	64.9
	0.75	1.1	1.8	2.5	1.9	1.8	3.7	3.3	4.4	5.5	6	7.4	8.75	11.6	13.1	14.8	28.2	29.9	32	55.8	57.6	60
1	0	1	1.5	1.9	1.8	1.5	3	3.1	3.8	4.5	5.8	6.6	7.45	11.1	11.9	13	27	27.9	29.1	53.5	54.3	55.7
	0.25	1.6	2.6	3.5	2.5	2.6	4.9	3.9	5.5	6.9	6.9	8.7	10.5	12.7	14.8	17.1	30.3	32.7	35.6	59.6	61.9	65.4
	0.5	1.6	2.3	3	2.4	2.3	4.2	3.8	4.9	6	6.5	7.9	9.26	12.1	13.6	15.3	27.5	30.3	32.5	56.4	58	60.5
	0.75	1.5	2	2.4	2.3	2	3.5	3.6	4.3	5	6.3	7.1	7.96	11.6	12.4	13.5	27.5	28.4	29.6	54	54.9	56.2

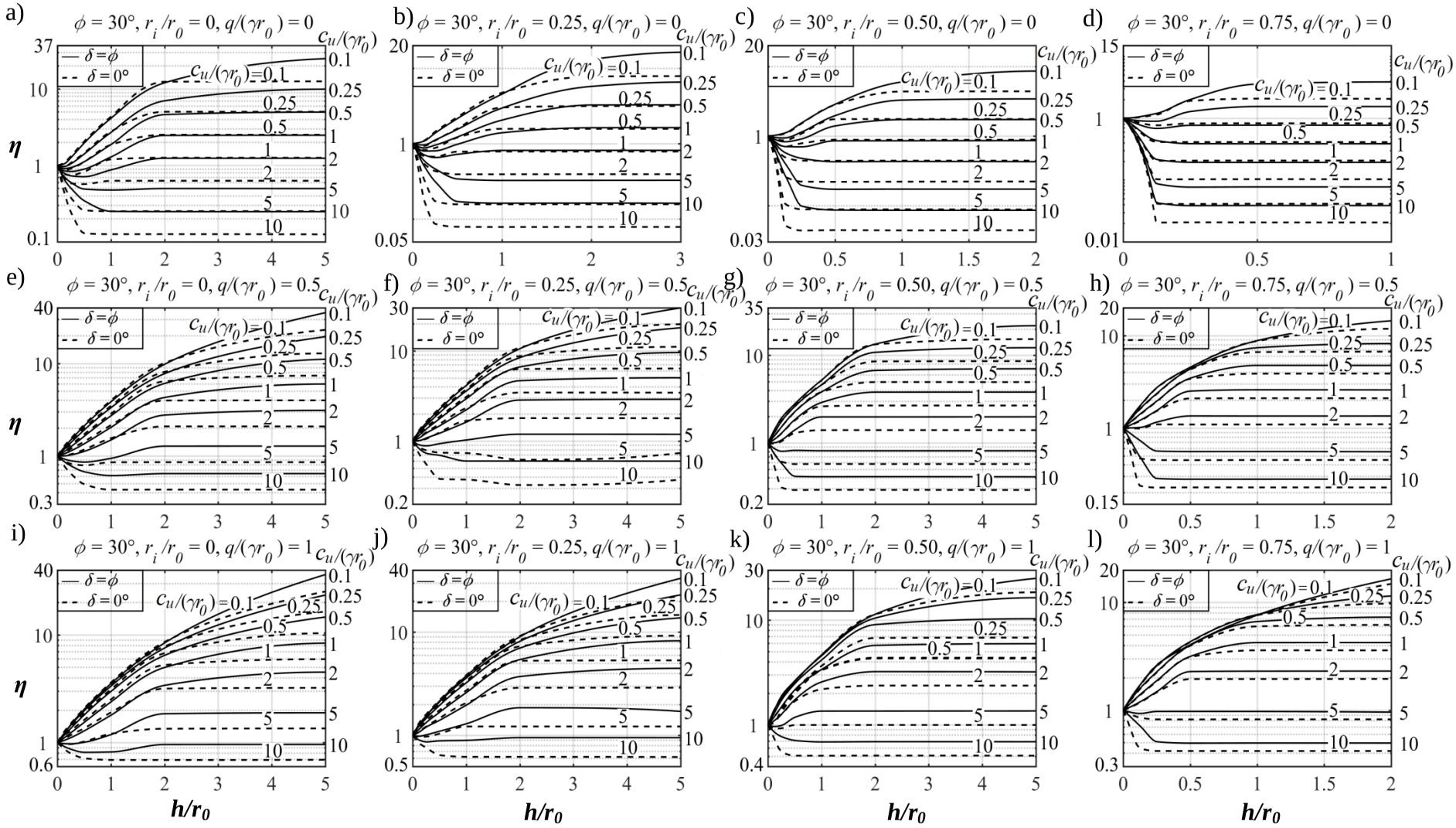

Figure 4.3 The variation of η with respect to h/r_0 for different smooth and rough annular footing resting on sands having ϕ= 30° and underlain by various homogenous cohesive stratum with varying surcharge: (a-d) $q/(\gamma r_0)$=0.0; (e-h) $q/(\gamma r_0)$=0.5; (i-l) $q/(\gamma r_0)$=1.0.

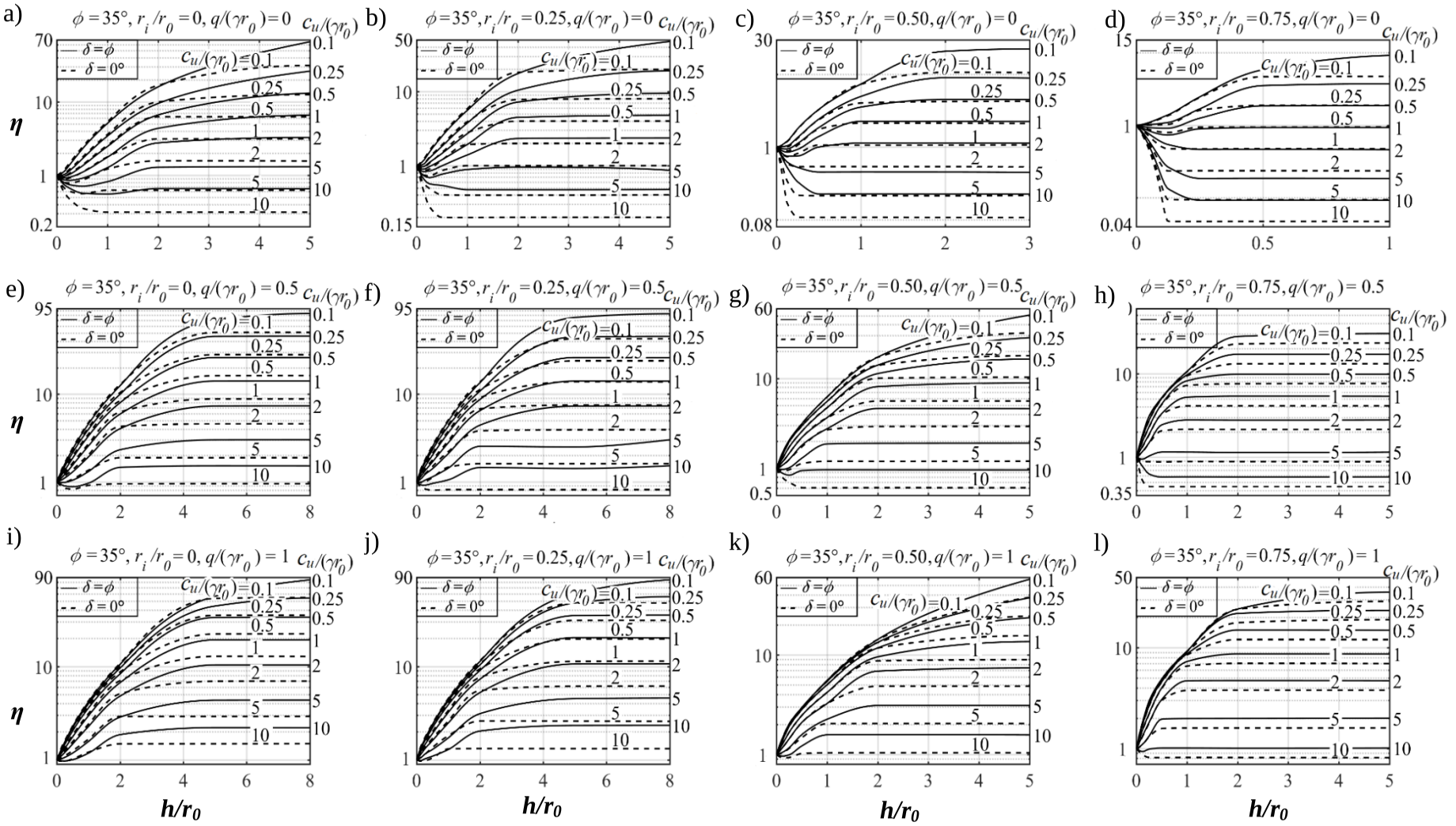

Figure 4.4 The variation of η with respect to h/r_0 for different smooth and rough annular footing resting on sands having ϕ= 35° and underlain by various homogenous cohesive stratum with varying surcharge: (a-d) $q/(\gamma r_0)$=0.0; (e-h) $q/(\gamma r_0)$=0.5; (i-l) $q/(\gamma r_0)$=1.0.

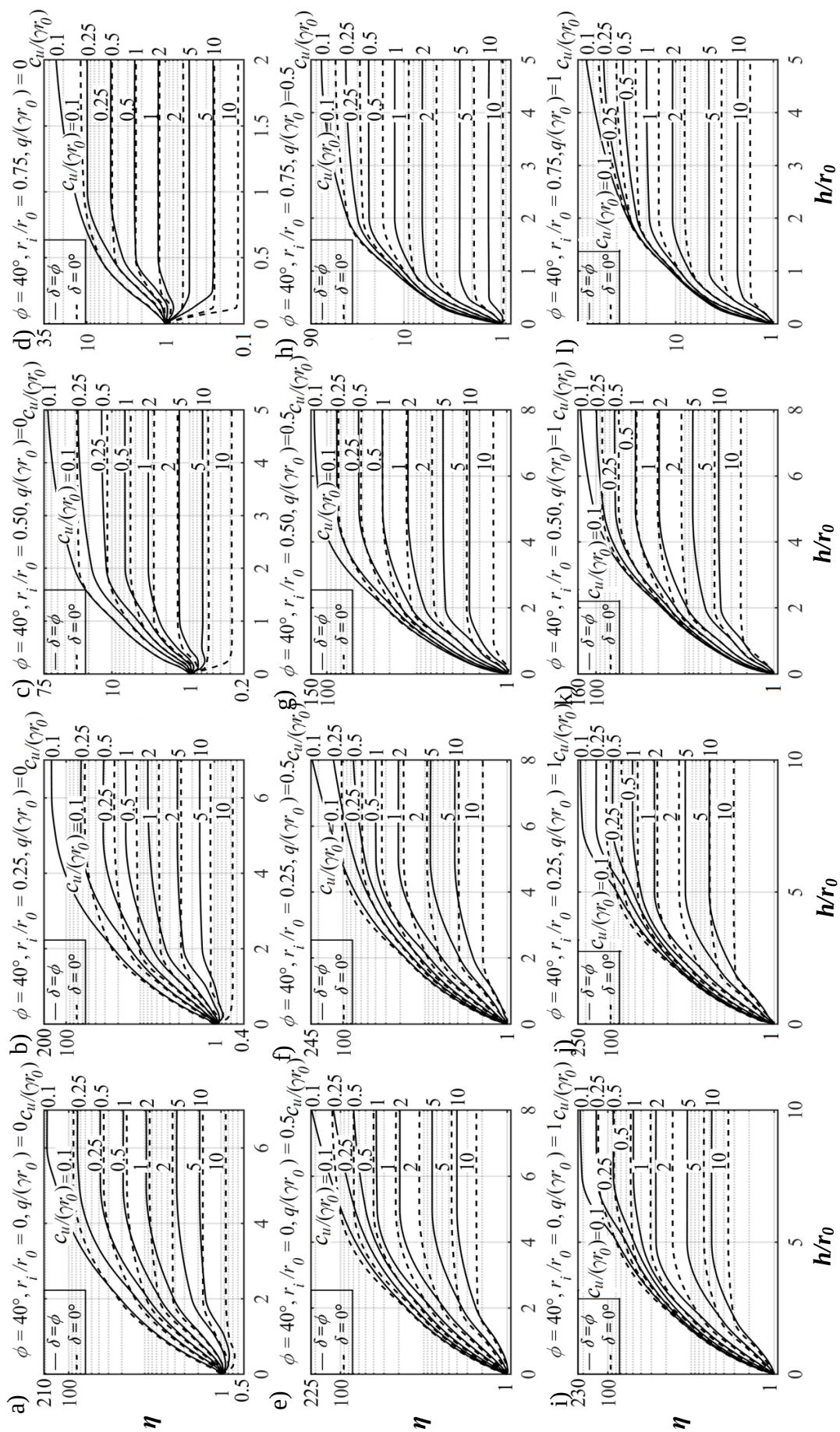

Figure 4.5 The variation of η with respect to h/r_0 for different smooth and rough annular footing resting on sands having ϕ= 40° and underlain by various homogenous cohesive stratum with varying surcharge: (a-d) $q/(\gamma r_0)$=0.0; (e-h) $q/(\gamma r_0)$=0.5; (i-l) $q/(\gamma r_0)$=1.0.

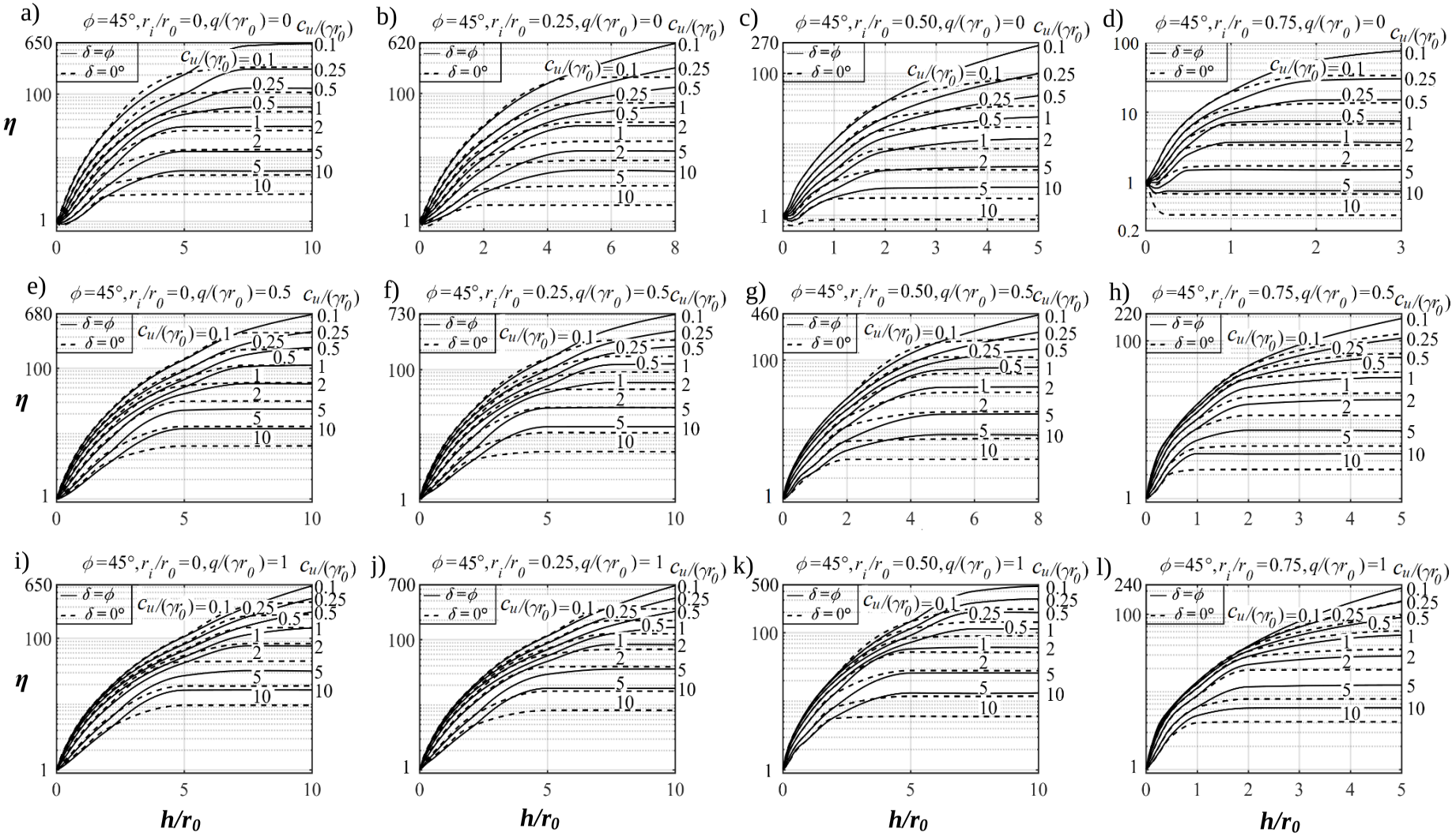

Figure 4.6 The variation of η with respect to h/r_0 for different smooth and rough annular footing resting on sands having ϕ= 45° and underlain by various homogenous cohesive stratum with varying surcharge: (a-d) $q/(\gamma r_0)$=0.0; (e-h) $q/(\gamma r_0)$=0.5; (i-l) $q/(\gamma r_0)$=1.0.

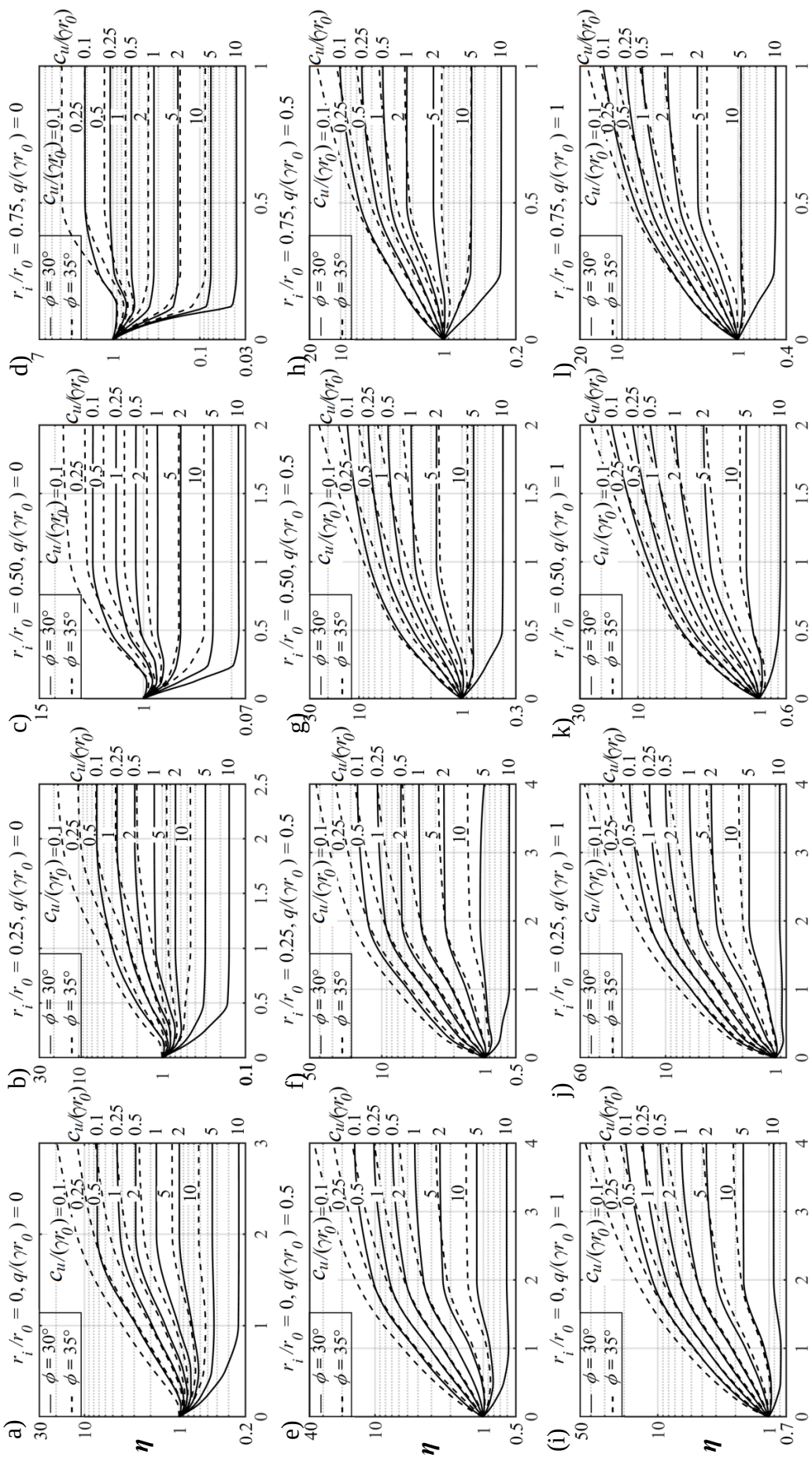

Figure 4.7 The variation of η with respect to h/r_0 for different annular footing corresponding to two different sands, ϕ= 30° and 35°, overlying on various cohesive layer having m=2 and subjected to varying surcharge: (a-d) $q/(\gamma r_0)$=0.0; (e-h) $q/(\gamma r_0)$=0.5; (i-l) $q/(\gamma r_0)$=1.0.

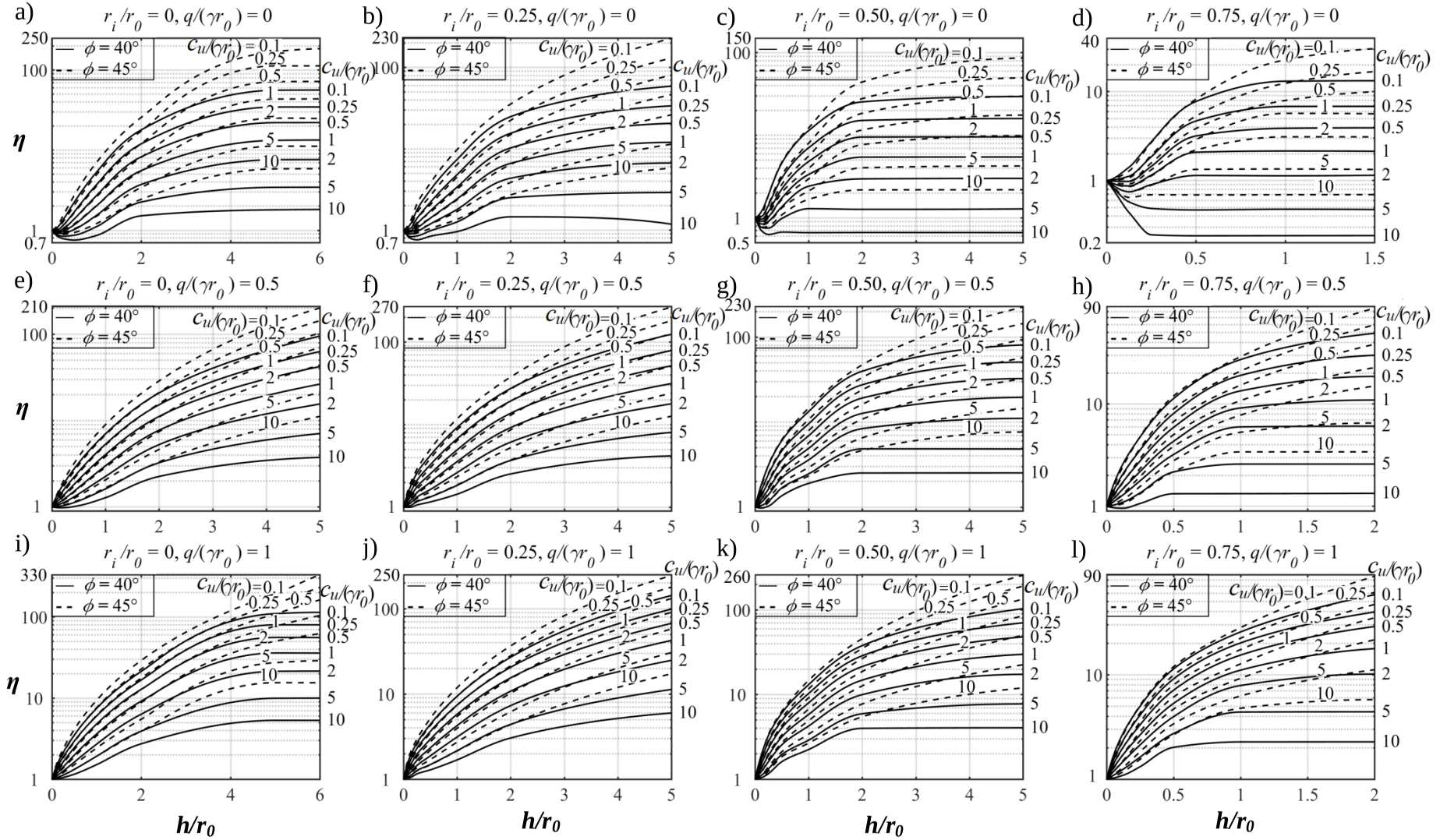

Figure 4.8 The variation of η with respect to h/r_0 for different annular footing corresponding to two different sands, ϕ= 40° and 45°, overlying on various cohesive layer having m=2 and subjected to varying surcharge: (a-d) $q/(\gamma r_0)$=0.0; (e-h) $q/(\gamma r_0)$=0.5; (i-l) $q/(\gamma r_0)$=1.0.

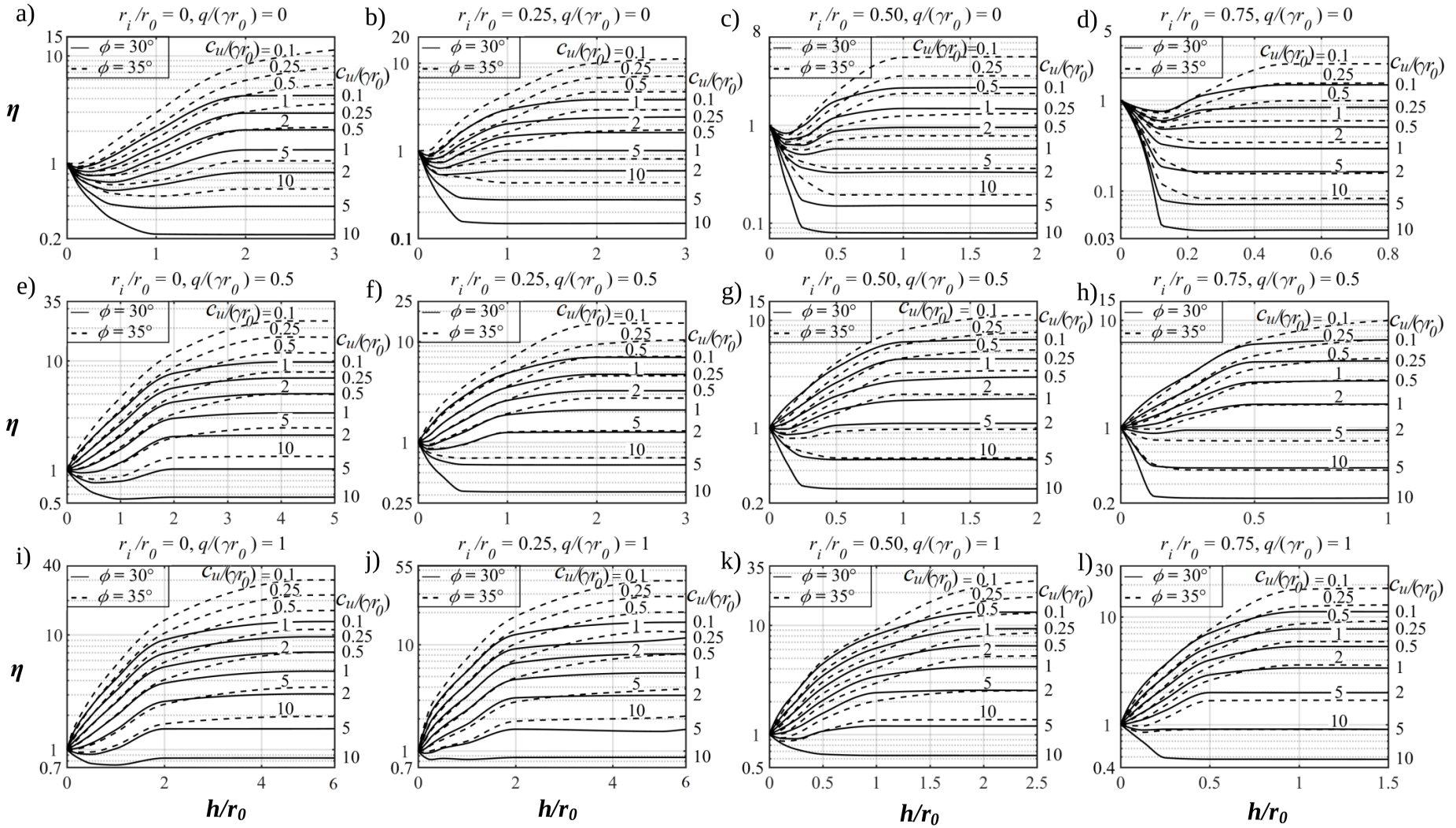

Figure 4.9 The variation of η with respect to h/r_0 for different annular footing corresponding to two different sands, ϕ= 30° and 35°, overlying on various cohesive layer having m=5 and subjected to varying surcharge: (a-d) $q/(\gamma r_0)$=0.0; (e-h) $q/(\gamma r_0)$=0.5; (i-l) $q/(\gamma r_0)$=1.0.

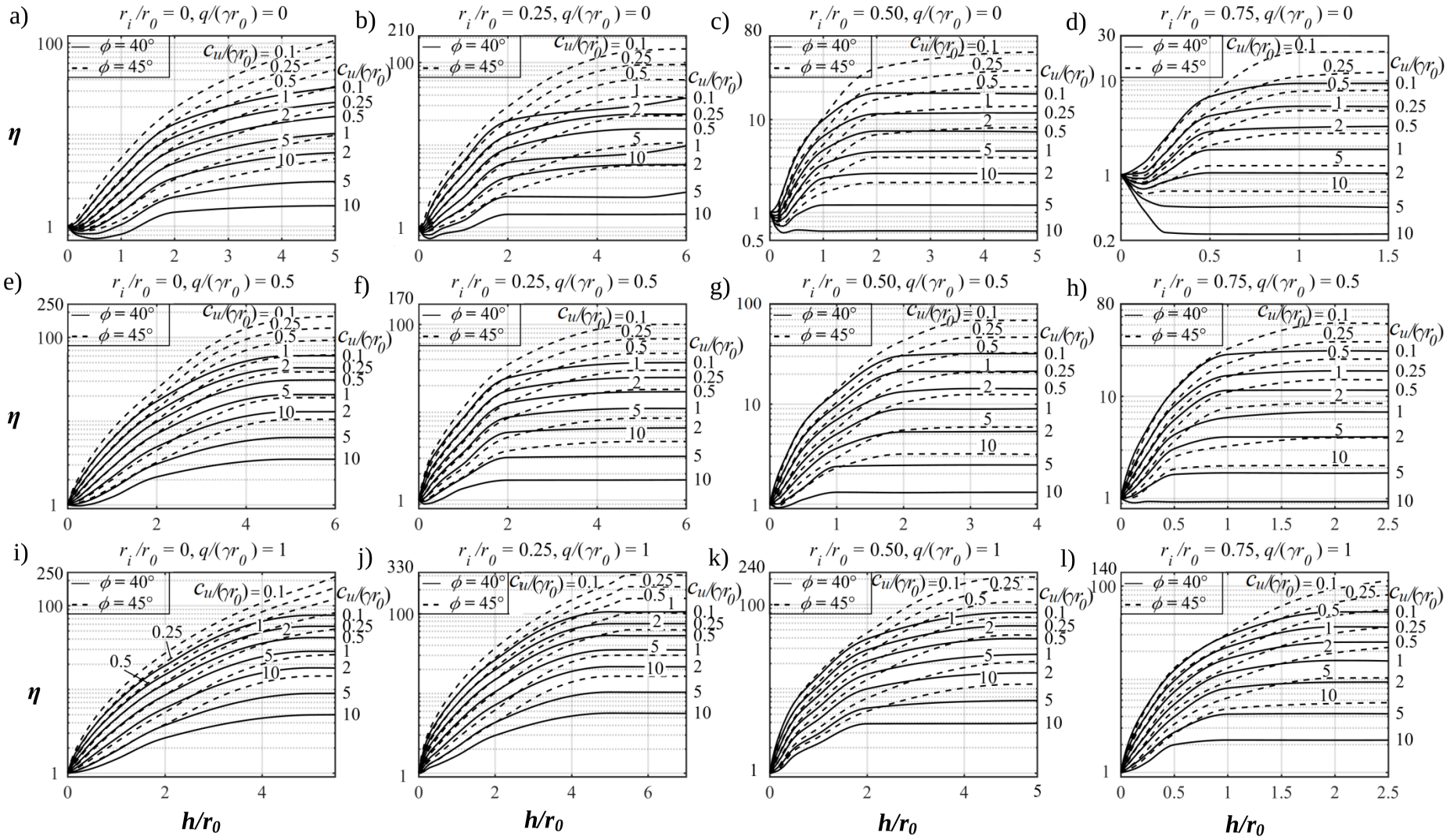

Figure 4.10 The variation of η with respect to h/r_0 for different annular footing corresponding to two different sands, ϕ= 40° and 45°, overlying on various cohesive layer having m=5 and subjected to varying surcharge: (a-d) $q/(\gamma r_0)$=0.0; (e-h) $q/(\gamma r_0)$=0.5; (i-l) $q/(\gamma r_0)$=1.0.

accordance with Atkinson (2007), the designation of clays as strong or weak is based solely on their strength values.

d) Depending on the combined effect of the surcharge loading, layer strength, and ring geometry, the curves representing the efficiency factors either increases or decreases with respect to the sand layer thickness. The magnitude of η changeswith h/r_0 upto a certain sand layer thickness, beyond which η becomes almost constant. This specific thickness of sand layer is termed here as *optimum thickness* and is denoted as, h_{opt}.

e) It can be noted from the figures that for a certain ring footing, the magnitude of h_{opt} seems to be highly dependent on the strength of the bottom clay layer. As $c_u/(\gamma r_0)$ increases, small amount of sand is required to be placed beneath the ring footing for attaining the maximum benefit.

f) Table 4.2 provides the variation of h_{opt}/r_0 with respect to the material properties (ϕ, $c_u/(\gamma r_0)$, and m), surcharge loading ($q/(\gamma r_0)$), geometrical configurations (r_i/r_0), and soil-footing roughness conditions (δ). It can be concluded that h_{opt}/r_0 increases with the increase in sand friction, surcharge pressure, and soil footing roughness. The difference of h_{opt}/r_0 for the smooth and the rough foundation is quite significant especially for lower surcharge and higher value of r_i/r_0. However, the required optimum thickness decreases with the increase in the cohesive strength and the r_i/r_0 ratios.

g) Figures 4.7 to 4.10 depict the variation of η corresponding to two values of cohesion increment rate (m), namely, 2 and 5. It is to be noted that with the increase in m, the efficiency factor decreases. The value of m also influences the optimum sand thickness; for an example, h_{opt}/r_0 decreases as m changes from 0 to 2 but remains almost the same for $m = 2$ and $m = 5$.

Table 4.2. The variation of h_{opt}/r_0 corresponding to $c_u/(\gamma r_0) = 1$ and for different values of ϕ, m, r_i/r_0, and $q/(\gamma r_0)$.

ϕ	r_i/r_0	h_{opt}/r_0								
		m=0			m=2			m=5		
		$q/(\gamma r_0)$ = 0.0	0.5	1.0	$q/(\gamma r_0)$ = 0.0	0.5	1.0	$q/(\gamma r_0)$ = 0.0	0.5	1.0
30°	0	2.00 (1.80)	4.6 (1.80)	5.00 (3.00)	1.80	3.00	3.50	2.00	3.00	4.00
	0.25	2.00 (0.50)	4.00 (2.00)	5.00 (2.00)	1.00	2.00	2.00	1.00	1.50	2.00
	0.50	0.50 (0.25)	1.80 (1.00)	3.00 (2.00)	0.50	1.00	1.50	0.50	1.00	1.50
	0.75	0.25 (0.125)	1.00 (0.50)	1.00 (0.80)	0.25	0.50	0.80	0.25	0.50	0.75
35°	0	5.00 (2.00)	5.00 (5.00)	4.50 (4.50)	3.00	5.00	5.00	2.50	3.50	4.50
	0.25	4.50 (1.00)	5.00 (2.00)	4.50 (4.00)	1.80	4.00	5.00	2.00	5.00	4.50
	0.50	1.00 (0.50)	3.00 (2.00)	4.00 (2.00)	1.00	2.50	5.00	1.50	1.00	2.00
	0.75	0.50 (0.125)	1.00 (1.00)	1.80 (1.00)	0.50	1.00	2.00	0.50	0.50	1.50
40°	0	4.80 (4.00)	5.00 (4.80)	7.50 (5.00)	4.80	5.00	5.00	5.00	5.00	5.00
	0.25	4.20 (3.00)	5.00 (4.50)	7.50 (5.00)	4.80	5.00	5.00	5.00	5.00	5.00
	0.5	2.00 (1.00)	5.00 (2.00)	5.00 (4.00)	2.50	5.00	5.00	3.00	2.00	5.00
	0.75	0.50 (0.25)	2.00 (1.00)	3.00 (2.00)	1.00	2.00	2.00	1.00	2.00	2.00
45°	0	7.50 (5.00)	7.50 (6.00)	10.00 (7.50)	5.00	7.50	7.50	5.00	7.50	7.50
	0.25	7.50 (4.50)	7.50 (4.50)	10.00 (5.00)	5.00	7.50	7.50	5.00	7.50	7.50
	0.50	4.50 (2.00)	4.50 (4.50)	7.50 (4.25)	5.00	2.00	7.50	5.00	5.00	5.00
	0.75	2.00 (1.00)	3.00 (2.00)	4.50 (2.00)	2.00	2.00	2.00	2.00	2.00	5.00

Note: The values inside and outside the parenthesis correspond to smooth and rough footing, respectively.

h) It is to be noted that η is higher for homogenous clays than the non-homogenous one having linearly increasing strength. Incorporating sands of higher friction and applying high surcharge pressure further improves the efficiency factor.

i) Table 4.3 presents the numerical efficiency factors corresponding to (i) three different cohesive strength of the bottom layer ($c_u/(\gamma r_0)$ = 0.1, 1.0, and 10), (ii) four different frictional strength of the top layer (ϕ = 30°, 35°, 40°, and 45°), (iii) three distinct sand layer thickness (h/r_0 = 0.25, 1, and 5), and (iv) four discrete radius ratio (r_i/r_0 = 0, 0.25, 0.50, and 0.75). This table is presented for constant surcharge loading and homogenous clays. It is well observed that the nature of the variation of η with respect to r_i/r_0 depends much on the frictional strength of

Table 4.3. The variation of η corresponding to $q/(\gamma r_0)$ = 0.5, m = 0, and for various combinations of ϕ, h/r_0, $c_u/(\gamma r_0)$, and r_i/r_0.

ϕ	r_i/r_0	$c_u/(\gamma r_0)$ = 0.1			$c_u/(\gamma r_0)$ = 1			$c_u/(\gamma r_0)$ = 10		
		h/r_0 =								
		0.25	1	5	0.25	1	5	0.25	1	5
30º	0	1.26	4.14	24.87	0.83	1.29	2.48	0.50	0.25	0.25
	0.25	1.38	4.54	16.28	0.80	1.39	1.63	0.31	0.16	0.16
	0.50	1.54	5.98	16.30	0.70	0.85	0.86	0.10	0.09	0.09
	0.75	2.00	3.86	16.27	0.39	0.39	0.39	0.04	0.04	0.04
35º	0	1.39	5.11	65.94	0.94	1.77	6.57	0.67	0.56	0.66
	0.25	1.52	5.59	47.57	0.97	1.93	4.77	0.57	0.47	0.48
	0.50	1.79	7.38	22.55	0.93	2.26	2.25	0.33	0.23	0.22
	0.75	2.46	9.17	9.22	0.89	0.93	0.93	0.09	0.09	0.09
40º	0	1.52	6.27	145.56	1.03	2.29	19.11	0.80	0.89	1.90
	0.25	1.66	6.87	138.96	1.11	2.51	16.65	0.77	0.98	1.57
	0.50	2.05	9.12	66.55	1.12	3.33	6.77	0.63	0.67	0.68
	0.75	2.95	14.22	24.44	1.26	2.46	2.47	0.25	0.24	0.25
45º	0	1.67	7.70	202.32	1.12	2.91	8.54	0.90	1.25	2.52
	0.25	1.83	8.42	222.33	1.22	3.19	9.37	0.93	1.37	2.75
	0.50	2.35	11.17	244.59	1.31	4.22	12.30	0.86	1.78	2.39
	0.75	3.49	19.72	75.45	1.59	7.09	7.46	0.74	0.74	0.74

the sand and sand layer thickness. If a thin to moderate thick sandy layer is installed between the ring footing and the weak clays, η increases with the increase in r_i/r_0 ratio, irrespective of the sand friction. However, if the thickness of the sandy layer is high, η decreases with the r_i/r_0 ratio especially for ϕ = 30°, 35°, and 40°; but, if the frictional strength of the sands is quite high (e.g. ϕ = 45°) the curve between η and r_i/r_0 turns into inverted 'V' shape profile manifesting a *specific radius ratio* ($r_{i,sp}/r_{0,sp}$) at which the efficiency factor is maximum. On the other hand, if the clay underneath the sandy layer is quite strong, the efficiency factor decreases with the r_i/r_0 ratio for thin sand layer. The magnitude of $r_{i,sp}/r_{0,sp}$ reduces with the increase in the strength of the clays. This overall observation finally suggests that the applications of sand over the weak clays are more advantageous for annular footing with certain r_i/r_0 ratio in comparison to the circular one.

j) Table 4.4 shows the influence of surcharge pressure on the variation of η with the r_i/r_0 ratio. The rate of increment of η with the r_i/r_0 ratio further enhances by the surcharge loading due to the placement of moderate thick layer of sand. The value of $r_{i,sp}/r_{0,sp}$ increases with the application of surcharge.

k) Figure 4.11 represents the variation of η with respect to the footing roughness, δ. The numerical simulations are carried out considering two different sands (ϕ = 30°, 40°) of optimum thickness placed over nine different clays ($c_u/(\gamma r_0)$ = 0.1, 1.0, and 10; m = 0, 2, and 5). The surcharge pressure is kept to be constant at $q/(\gamma r_0)$ = 1. The curves depict that with the improvement of footing roughness, there is an enhancement of the efficiency factor up to a certain δ/ϕ value; beyond that η remains constant. This figure also shows that placing of strong sands over

weak clays is more beneficial for r_i/r_0 = 0.25 in comparison to the circular one; and, this effect becomes more prominent for higher m.

Table 4.4. The variation of η corresponding to $c_u/(\gamma r_0)$ = 0.5, m = 0, and for various combinations of ϕ, h/r_0, $q/(\gamma r_0)$, and r_i/r_0.

ϕ	r_i/r_0	$q/(\gamma r_0)$ = 0			$q/(\gamma r_0)$ = 0.5		
		h/r_0 =					
		0.5	2	10	0.5	2	10
30º	0	1.12	4.61	4.97	1.63	6.07	11.09
	0.25	1.22	3.25	3.25	1.77	6.62	10.35
	0.50	1.39	1.72	1.72	2.28	6.72	7.02
	0.75	0.77	0.77	0.77	3.46	4.75	4.76
35º	0	1.34	6.65	13.15	1.87	8.01	26.32
	0.25	1.46	7.23	9.5	2.02	8.73	26.11
	0.50	1.85	4.53	4.5	2.58	11.35	16.39
	0.75	1.85	1.85	1.84	4.34	9.84	9.88
40º	0	1.56	8.94	38.13	2.14	10.38	68.95
	0.25	1.71	9.85	31.15	2.32	11.31	74.24
	0.50	2.26	11.76	13.63	3.01	14.78	43.78
	0.75	3.44	4.9	4.89	5.25	22.74	23.01
45º	0	1.81	11.87	123.53	2.45	10.51	205.63
	0.25	1.99	13	123.5	2.66	11.5	224.86
	0.50	2.63	17.24	47.67	3.46	15.12	142.37
	0.75	4.42	14.85	14.96	6.06	25.31	62.4

4.5 FAILURE PATTERNS

After the lower bound limiting state is attained, the failure patterns are drawn by using the stress components (σ_r, σ_z, σ_θ and τ_{rz}) obtained at each node. By using the stress components, the principal stresses σ_1 and σ_3 at each node are obtained by employing the following expressions:

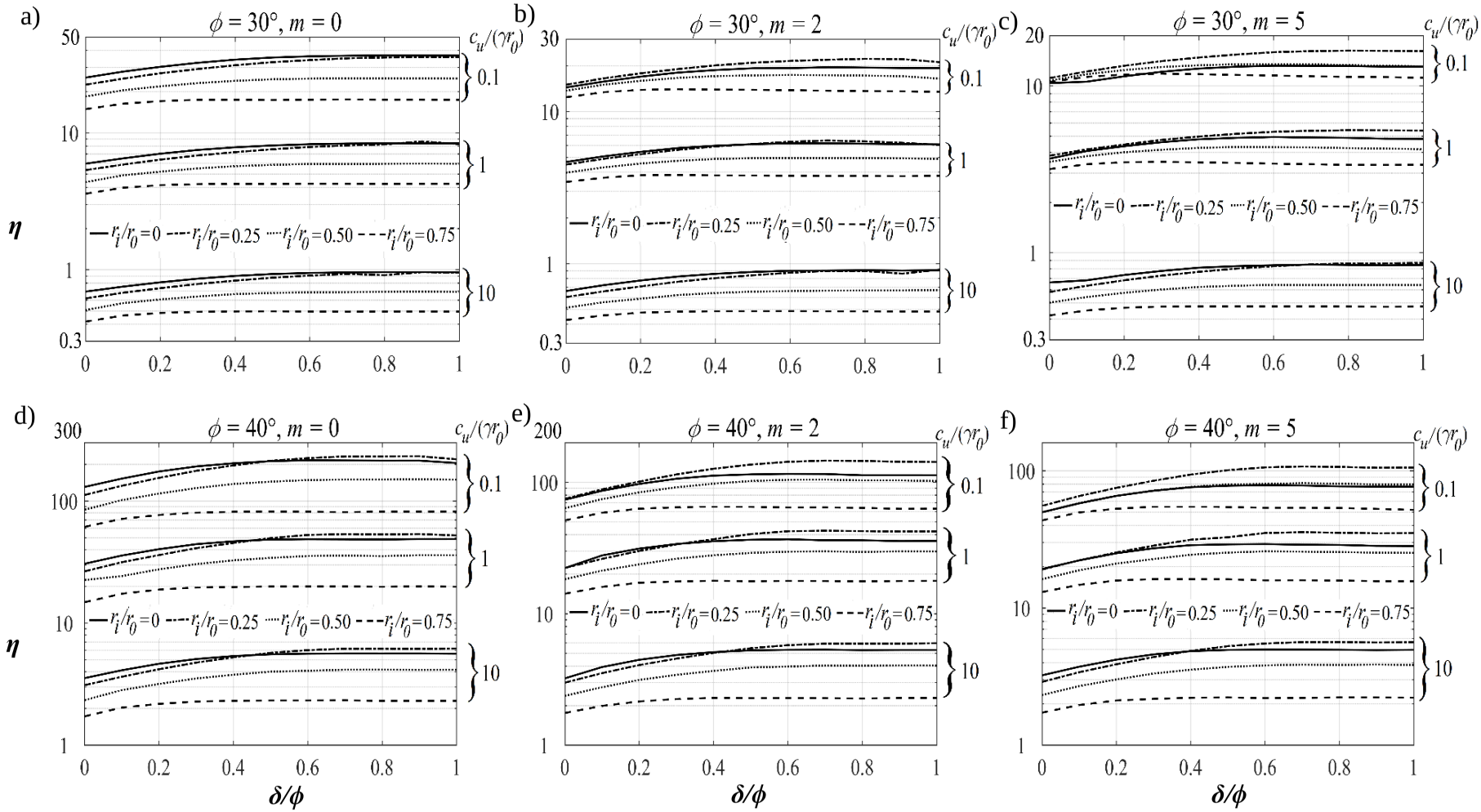

Figure 4.11 The variation of η with respect to footing roughness corresponding to three different $c_u/(\gamma r_0)$, namely, 0.1,1.0, and 10 with optimum sand thickness and for following different cases: a) ϕ = 30°, m=0; b) ϕ = 30°, m=2; c) ϕ = 30°, m=5; d) ϕ = 40°, m=0; e) ϕ = 40°, m=2; and f) ϕ = 40°, m=5.

$$\sigma_1, \sigma_3 = \frac{\sigma_r + \sigma_z}{2} \pm \sqrt{\left(\frac{\sigma_r - \sigma_z}{2}\right)^2 + \tau_{rz}^2} \tag{4.4}$$

The proximity of a point to shear failure can be computed by evaluating the *a/d* ratio through the following expressions:

$$a = \left(\frac{\sigma_{\max} - \sigma_{\min}}{2}\right)^2 + \tau^2; \quad \text{If}, \sigma_{\max} \geq \sigma_\theta \geq \sigma_{\min}\ ,\ \tau = \tau_{rz} \text{ or else } \tau = 0 \tag{4.5a}$$

$$d = \left\{-\left(\frac{\sigma_{\max} + \sigma_{\min}}{2}\right)^2 + c\cot\phi\right\}^2 \sin^2\phi \qquad \text{(for sand layer)} \tag{4.5b}$$

$= c_u\,(z)$ as mentioned in Equation (4.1) (for clay layer)

where, $\sigma_{\max}\,(/\sigma_{\min})$ = max (/min) of $(\sigma_1, \sigma_3, \text{ and } \sigma_\theta)$

Here, *a* and *d* denote the square of the radius of the Mohr circle at the current limiting state and the failure state, respectively. The failure patterns are drawn by varying the brightness of the colour map on the basis of the computed *a/d* ratio. The pitch-dark portion in the failure contours indicates the plastic shear failure zone (i,e, *a/d* = 1). On the other hand, *a/d*<1 indicate that the stress state of that point will be non-plastic. The detailed procedure of calculating *a* and *d* for axisymmetric footing can be seen in the work of Kumar and Chakraborty (2015).

Figures 4.12–4.18 shows the impact of frictional strength, cohesive strength (considering homogenous clays), sand layer thickness, radius ratios, footing roughness, surcharge pressure, and cohesive strength increment rate (considering non-homogenous clays), respectively. The footing surface is considered to be rough for all the cases, except Figure 4.16. The following observations are made from these figures:

a) Figure 4.12 depicts that the size of the plastic zone expands significantly with the increase in strength of the sand. For ϕ = 30°, the plastic zone which appears to be only in the top layer starts to enter into the bottom clays for $\phi \geq 35°$. With

the increase in ϕ, the non-plastic rigid wedge developed below the footing base also grows in size.

b) For a certain sand layer, with the increase in the cohesive strength of the bottom layer, the plastic zone starts to shrink and finally contains only within the top layer, as shown in Figure 4.13. The size of the elastic wedge beneath the footing also reduces with the strengthening of the bottom clays. It can be further inferred that the strong clays which restricts the failure zone only in the top portion, would not collapse until the top layer becomes completely unstable. The extent of failure zone substantiates the cause of lower efficiency factor for strong clays. The size of the elastic wedge developed beneath the footing base grows either by increasing ϕ and/or by decreasing c_u.

c) Figure 4.14 presents the influence of the sand layer thickness on the failure contours. It is observed that after a certain h, the failure zone gets confined solely within the sandy layer. This observation establishes the cause of the optimum thickness.

d) Figure 4.15 presents the influence of the radius ratio on the failure contours. For the considered combination of material properties, the size of the failure domain appears to be maximum for $r_i/r_0 = 0.25$ and reduces considerably for $r_i/r_0 = 0.75$.

e) The variation of the failure domain with r_i/r_0 ratio further explains the existence of $r_{i,sp}/r_{0,sp}$.

f) Figure 4.16 clearly reveals that the size of the failure domain, especially in the vertical direction, increases with the increase in footing roughness. The variation of the failure domain is more prominent when δ varies from 0 to 0.25ϕ; however, when δ/ϕ changes between 0.4 and 0.6, the change seems to be insignificant.

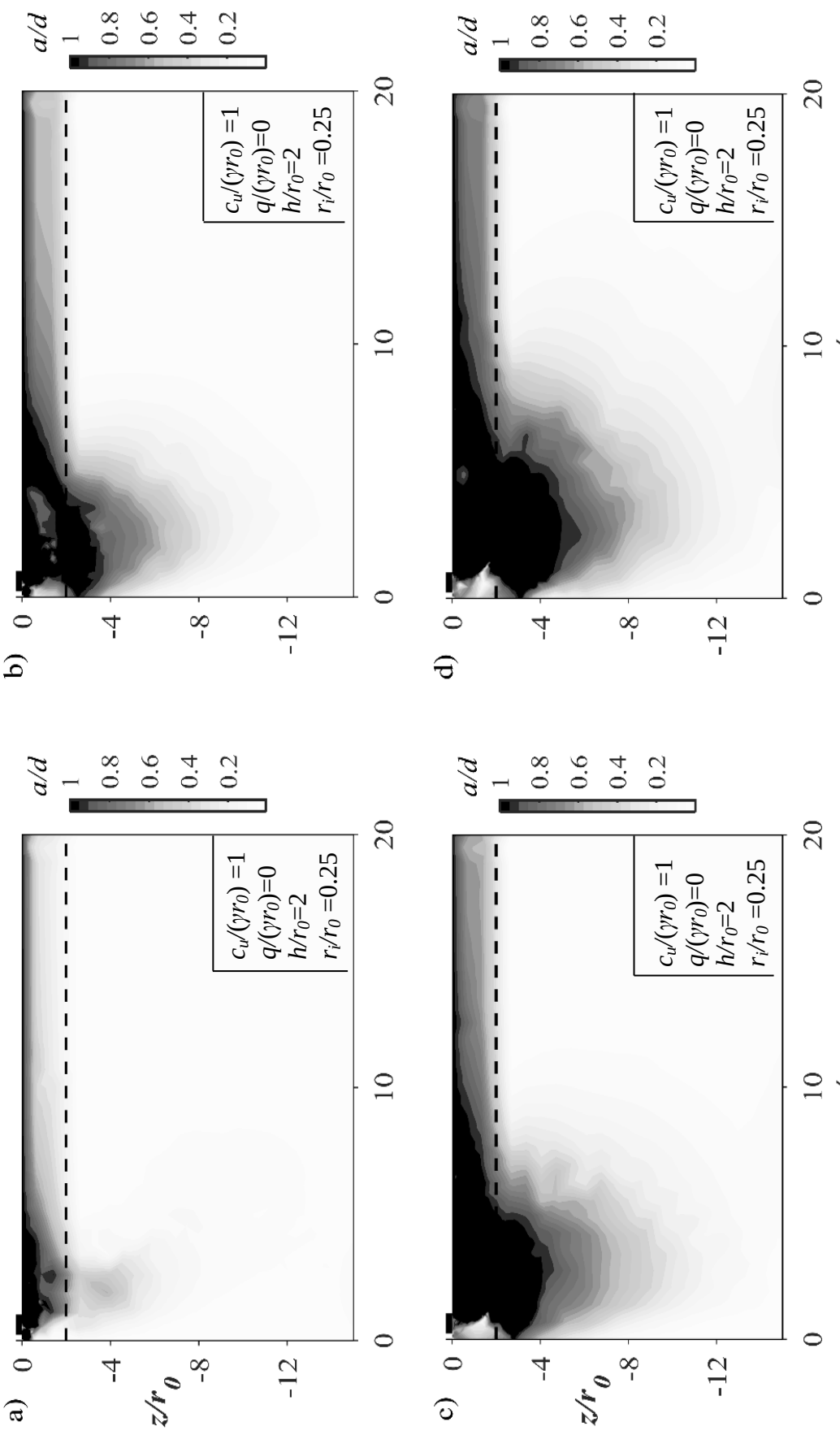

Figure 4.12 Failure pattern for $c_u/(\gamma r_0)$ =1, $q/(\gamma r_0)$=0, h/r_0=2, and r_i/r_0 =0.25 with various value of ϕ: a) ϕ=30°; b) ϕ=35°; c) ϕ=40°; and d) ϕ=45°.

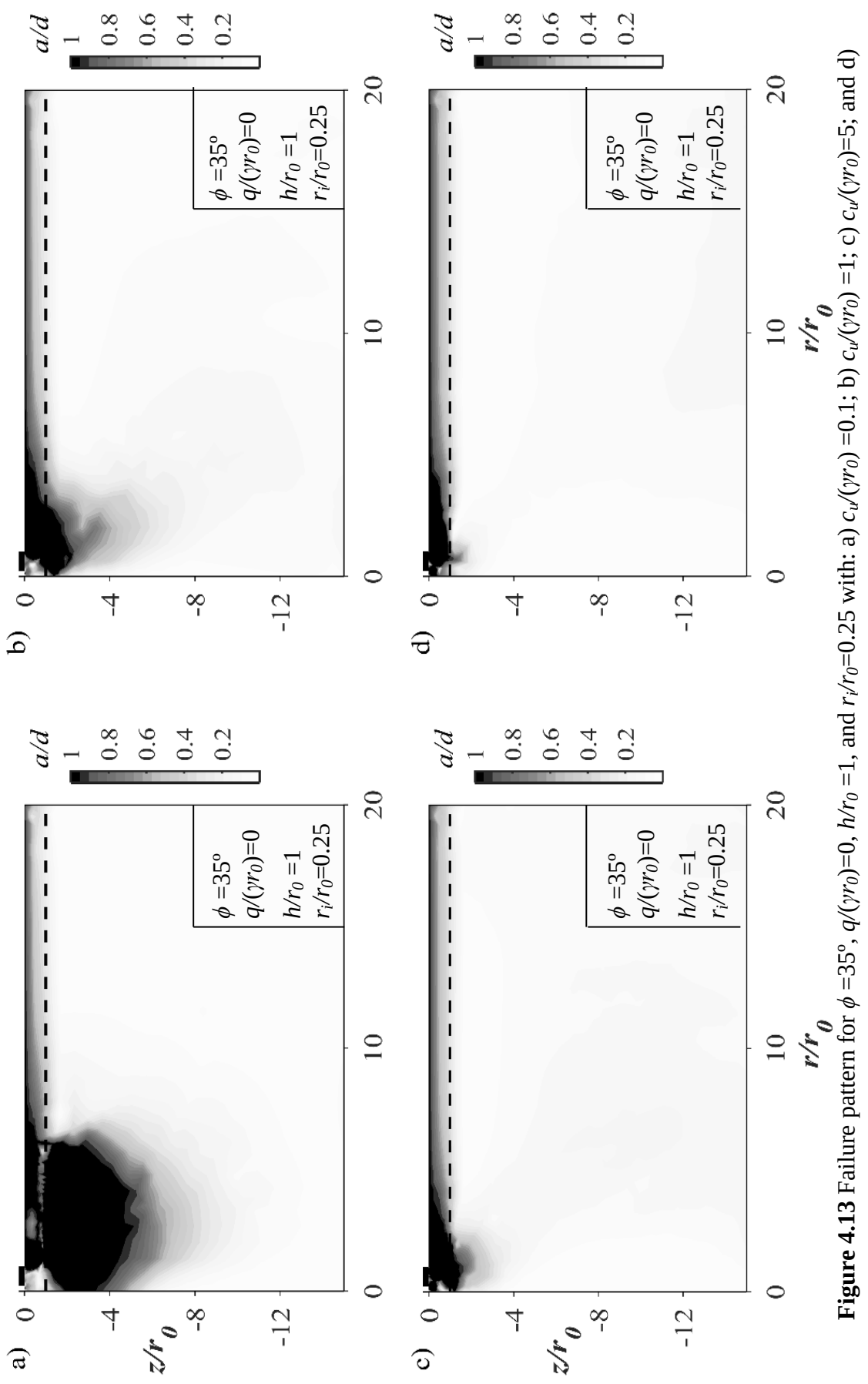

Figure 4.13 Failure pattern for ϕ =35°, $q/(\gamma r_0)$=0, h/r_0 =1, and r_i/r_0=0.25 with: a) $c_u/(\gamma r_0)$ =0.1; b) $c_u/(\gamma r_0)$ =1; c) $c_u/(\gamma r_0)$=5; and d) $c_u/(\gamma r_0)$=10.

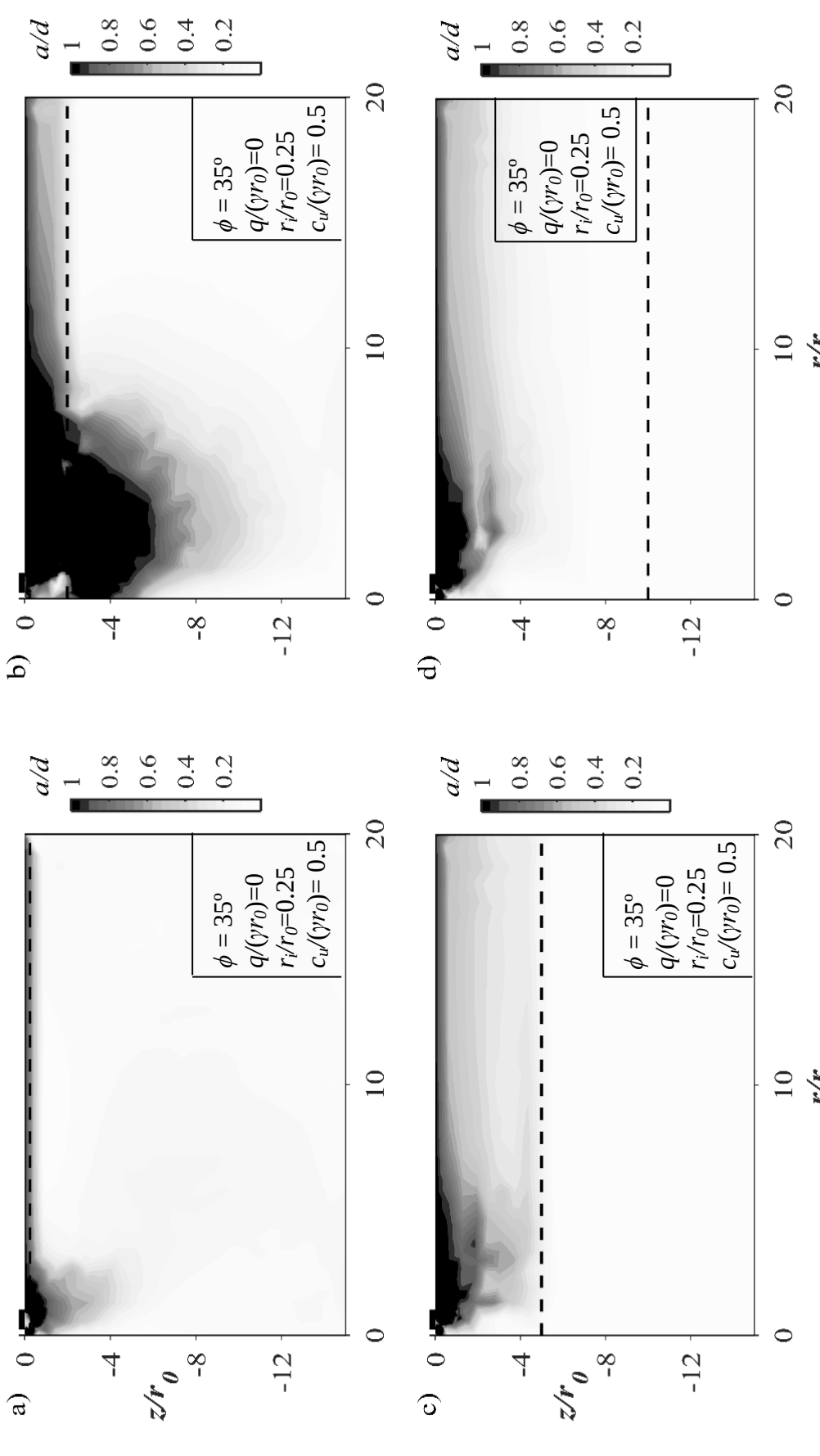

Figure 4.14 Failure pattern for $\phi = 35°$, $q/(\gamma r_0)=0$, $r_i/r_0=0.25$, and $c_u/(\gamma r_0)= 0.5$ corresponding to: a) $h/r_0= 0.25$; b) $h/r_0 =2$; c) $h/r_0 =5$; and d) $h/r_0= 10$.

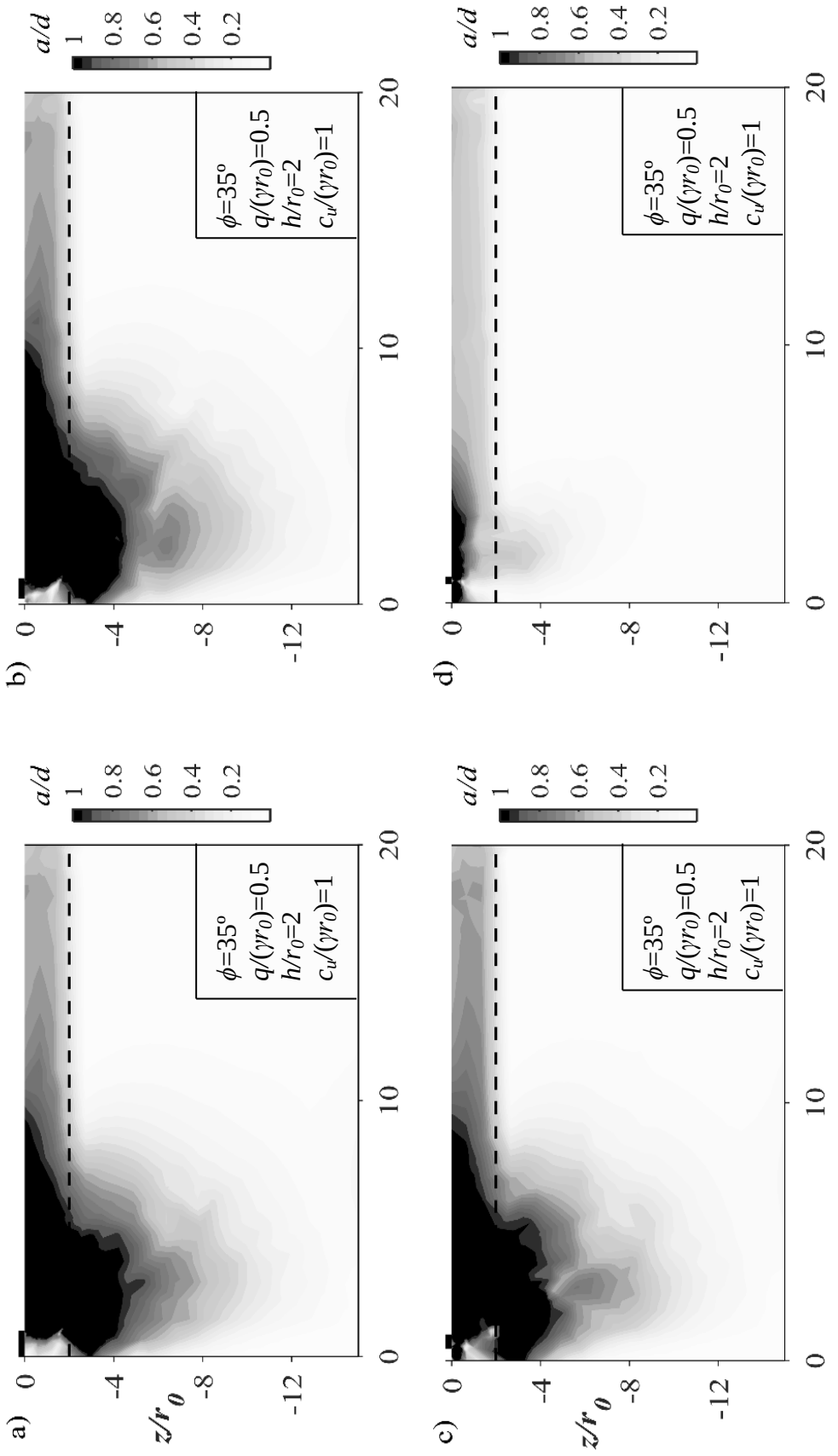

Figure 4.15 Failure pattern for ϕ=35°, $q/(\gamma r_0)$=0.5, h/r_0=2, and $c_u/(\gamma r_0)$=1 with: a) r_i/r_0= 0; b) r_i/r_0=0.25; c) r_i/r_0=0.5; and d) r_i/r_0=0.75.

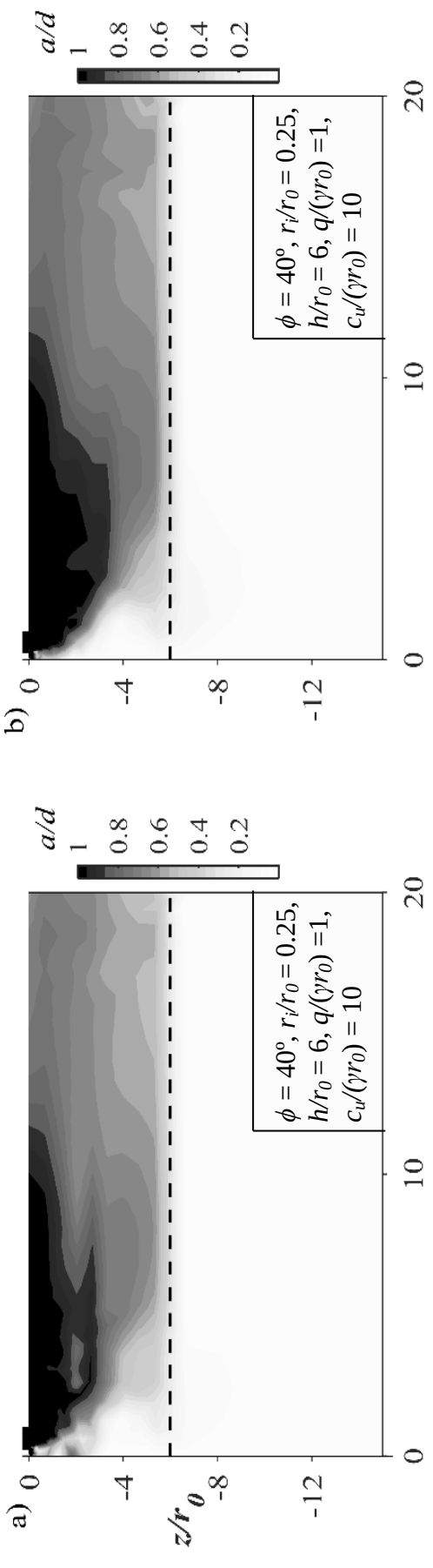

Figure 4.16 Failure pattern for $\phi = 40°$, $r_i/r_0 = 0.25$, $h/r_0 = 6$, $q/(\gamma r_0) = 1$, and $c_u/(\gamma r_0) = 10$ with: a) $\delta/\phi = 0$; b) $\delta/\phi = 0.2$; c) $\delta/\phi = 0.4$; and d) $\delta/\phi = 0.6$.

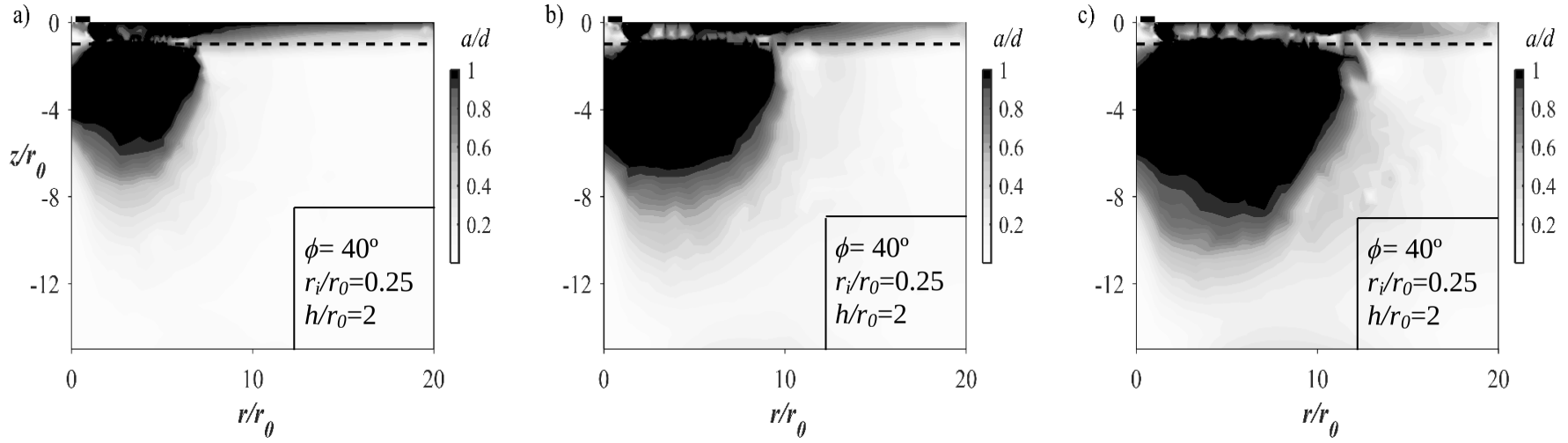

Figure 4.17 Failure pattern for ϕ= 40º, r_i/r_0=0.25, h/r_0=2, and $c_u/(\gamma r_0)$= 0.1 with: a) $q/(\gamma r_0)$= 0; b) $q/(\gamma r_0)$=0. 5; and c) $q/(\gamma r_0)$= 1.

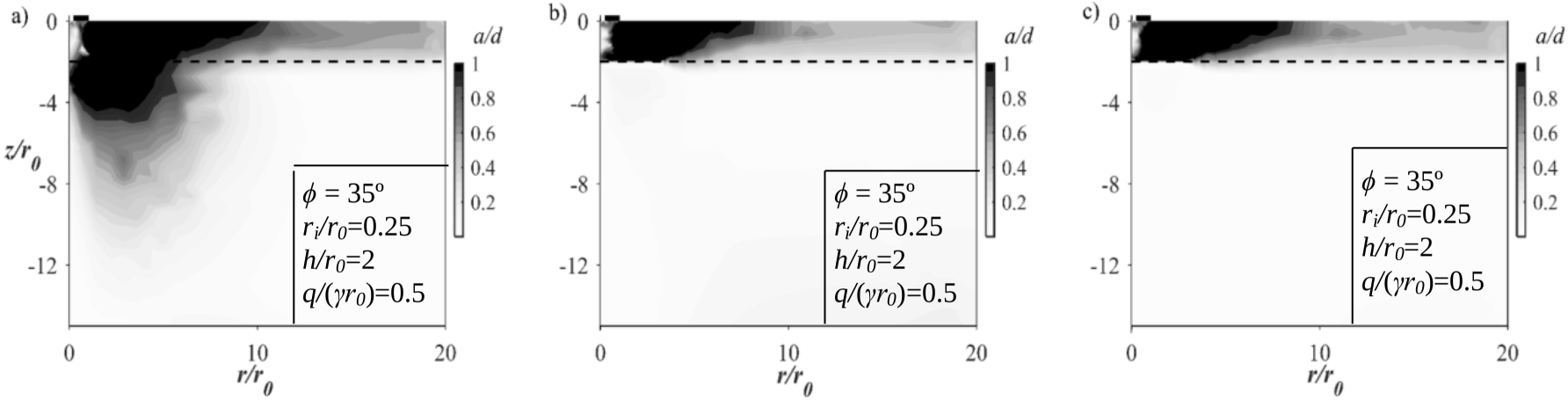

Figure 4.18 Failure pattern for ϕ = 35º, r_i/r_0=0.25, h/r_0=2, $q/(\gamma r_0)$=0.5, and $c_u/(\gamma r_0)$= 1 with: a) m= 0; b) m=2; and c) m= 5.

g) Figures 4.17 and 4.18 depict the impact of surcharge pressure and the cohesion increment rate on the failure contours. It is clearly observed that with the increase in *q*, failure domain encompasses larger portion of the clayey deposits and with the increase in *m*, volume of the plastic zone reduces. The variation of the failure contour is much more notable when *m* increases from 0 to 2 in comparison to 2 to 5.

4.6 COMPARISONS OF RESULTS

4.6.1 Comparisons of the Bearing Capacity of Circular Footing

4.6.1.1 For homogenous clays

Table 4.5 presents the comparison of the N_c values obtained from the present analysis for undrained saturated clays with the available solutions obtained on the basis of (i) finite- element lower-bound linear (Kumar and Chakraborty, 2015) and nonlinear (Salgado et al., 2004; Yang et al., 2020) analysis, (ii) upper-bound analysis by using FEM (Salgado et al., 2004; Yang et al., 2020) and rigid block method (Kusakabe et al., 1986), (iii) analytical method (Meyerhof, 1951), (iv) semiempirical methods (Skempton, 1951; Hansen, 1970; Vesic, 1973), (v) stress characteristics method (Tani and Craig, 1995; Houlsby and Martin, 2003; Martin, 2004), (vi) FEM (Edwards et al., 2006; Taiebat and Carter, 2010; Lee et al., 2016), and (v) experimental solution (Skempton, 1951; Dash et al., 2003; Demir et al., 2014). The N_c value reported by Meyerhof (1951), based on wedge failure mechanism, is higher than the solutions obtained from the present analysis. Skempton (1951) and Vesic (1973) modified the classical Terzaghi's bearing capacity in order to accommodate various shapes of foundations; similarly, Hansen (1970) proposed converting the bearing capacity factor2005; Gourvenec et al., of the square footing to a circular footing based on the equivalent footing area. The N_c value obtained by Hansen (1970) and Vesic (1973) is

more than the present N_c value, whereas the N_c value obtained by Skempton (1951) is found to be bit lower. Except for the solution produced by Gourvenec et al. (2006), the

Table 4.5. A comparison of N_c for rough circular footing (r_i/r_0 = 0) resting on homogenous clay.

Methods			References	N_c
Limit Analysis	Finite Element Lower Bound	IPM	Present Analysis	6.02
		Linear	Kumar and Chakraborty (2015)	6.00
		Non-Linear	Salgado et al. (2004)	5.86
			Yang et.al. (2020)	6.02
	Upper Bound	Rigid Block	Kusakabe et al. (1986)	6.31
		Finite Element	Salgado et al. (2004)	6.23
			Yang et.al. (2020)	6.06
Analytical Method			Meyerhof (1951)	6.05
Semi-Empirical Method			Skempton (1951)	6.00
			Hansen (1970)	6.17
			Vesic (1973)	6.17
Method of Stress Characteristics			Tani and Craig (1995)	6.34
			Houlsby and Martin (2003)	6.05
			Martin (2004)	6.05
Finite Element Method			Edwards et al. (2005)	6.09
			Gourvenec et al. (2006)	5.96
			Taiebat and Carter (2010)	6.17
			Lee et al. (2016)	6.08
Experimental/Field test			Skempton (1951)	6.18
			Dash et al. (2003)	6.43
			Demir et al. (2104)	6.20

present N_c value is found to be lower than the solutions obtained by employing the method of stress characteristics, FEM, and experimental solution. This can be attributed to the lower-bound nature of the problem. It is also noted that the present nonlinear lower-bound method shows an improvement in the computation of N_c values in comparison with the previous lower-bound solutions (Kumar and Chakraborty, 2015; Salgado et al., 2004).

4.6.1.2 For homogenous cohesionless sand ($\phi_u = 0^o$)

The N_γ values computed from the present analysis for four different sands, namely, ϕ = 30°, ϕ = 35°, ϕ = 40°, and ϕ = 45°, are compared with the solutions obtained by (i) finite element limit theorem with the aid of Optum G2 (Khatri et al., 2017), interior point method alongwith the smoothened yield criterion (Chakraborty and Kumar, 2014), linearizing the yield criterion (Khatri and Kumar, 2011) and three dimensional structures (Lyamin et. al., 2007) (ii) displacement based elastoplastic finite element method (Loukidis and Salgado, 2009) (iii) method of stress characteristics (Martin, 2004; De Simone, 1985), and (iv) finite difference code, FLAC (Erickson and

Table 4.6. A comparison of N_γ for rough circular footing (r_i/r_0 = 0) resting on homogenous sands.

ϕ	Present work[a]	Khatri et al. (2017)[b]	Chakraborty and Kumar (2014)[a]	Khatri and Kumar (2011)[c]	Lyamin et. al. (2007)[d]	Loukidis and Salgado (2009)[e]	Martin (2004)[f]	De Simone (1985)[f]	Erickson and Drescher (2002)[g]
30°	14.95	14.82 (15.63)*	14.80	14.65	14.10 (19.84)	15.80	15.54	15.73	--
35°	39.95	39.77 (42.07)	40.10	39.97	37.18 (52.51)	42.00	41.97	42.38	45
40°	116.13	115.71 (124.31)	116.70	116.20	106.60 (157.2)	122.20	124.1	124.4	130
45°	378.87	379.62 (419.57)	380.08	379.79	338.00 (539.2)	408.50	419.4	418.9	456

Note: 1. a: The solutions are obtained on the basis of finite element lower bound with the help of interior point method.
b: The solutions are obtained on the basis of limit theorems by using the Optum G2 software
c: The solutions are obtained on the basis of limit theorems by employing finite elements and linearizing the Mohr-Coulomb criterion
d: The solutions are obtained on the basis of limit theorems applied on the three-dimensional circular structure
e: The solutions are obtained by using displacement based elastoplastic finite element method
f: The solutions are obtained by using Method of Stress Characteristics
g: The solutions are obtained by finite difference code, FLAC
2. * The values within and outside the parenthesis indicate the upper and lower bound solutions, respectively.

Drescher, 2002). The circular rough footing is assumed to be rested on homogenous sands. The comparisons are presented in Table 4.6. The present N_γ values compare closely with the nonlinear LB solutions of Chakraborty and Kumar (2014); a slight difference between the two solutions may be due to the use of (i) different version of Matlab software (ii) different chosen meshes, and (iii) difference tolerance level in optimization process. The differences in LB and UB N_γ values reported by Khatri et al. (2017) are found to be quite smaller than the corresponding differences outlined in the work of Lyamin et al. (2007). The solutions obtained on the basis of finite difference, finite element and the stress characteristics appear to be greater than the present bearing capacity factors. The N_γ values from the stress characteristics are closer to the UB values whereas, FLAC solutions are found to be even greater than the UB values.

4.6.1.3 For layered soil:- sand over clays

The comparison of the ultimate bearing capacity of circular footing resting over sands (having ϕ = 40°) and underlaid by clays are presented in Table 4.7 corresponding to different values of h/r_0 and $c_u/(\gamma r_0)$. The present results are compared with the solutions given by (i) Yang et al. (2020) obtained from Optum G2, (ii) Okamura et al. (1997) based on centrifuge test and (iii) Okamura et al. (1998) based on limit equilibrium method. The present solutions match quite well with the LB solutions provided by Yang et al. (2020). For higher value of $c_u/(\gamma r_0)$, the magnitude of $p_u/(\gamma r_0)$ reported from the non-rigorous limit equilibrium method appears to be quite higher than the present solutions.

4.6.2 Comparisons for ring footing

A comparison has been presented in Table 4.8 for ring footing placed on homogenous sand layer with ϕ = 20°, 25°, 30°, 40°, and r_i/r_0 = 0.25, 0.5, 0.75. The

present N_γ values are compared with the results provided by (i) Kumar and Chakraborty (2015), Tang and Phoon (2018) on the basis of lower bound limit analysis (ii) Kumar

Table 4.7. A comparison of $p_u/(\gamma r_0)$ for circular footing (r_i/r_0= 0, r_0 = 1.5m, and ϕ = 40º) resting over sand-clay medium with different values of h/r_0 and $c_u/(\gamma r_0)$.

h/r_0	$c_u/(\gamma r_0)$	Present work[a]	Yang et al. (2020)[b]	Okamura et al. (1997)[c]	Okamura et al. (1997)[d]
0	1.61	9.70	9.70 (9.76)	10.00	10.71
	3.01	18.12	18.14 (18.24)	--	19.27
	5.15	31.01	30.03 (31.21)	--	32.88
	6.26	37.75	37.71 (37.94)	--	39.12
1	0.75	11.80	11.82 (12.04)	--	10.69
	3.05	26.58	26.47 (27.14)	28.90	31.57
	5.19	36.04	36.60 (37.66)	--	52.45
	6.26	40.92	41.08 (42.27)	--	62.61
2	0.80	34.04	33.98 (34.85)	31.95	25.23
	1.20	40.56	40.42 (41.51)	37.01	31.98
	3.21	60.70	60.34 (62.40)	58.30	58.43
	5.15	73.65	73.29 (76.05)	73.30	87.12
	6.11	78.78	--	--	100.62
	7.78	86.68	--	--	124.25
3	2.45	107.61	106.62 (111.14)	--	84.65
	3.54	115.47	111.53 (125.53)	103	103.75
	5.84	115.15	114.89 (125.80)	141	152.05

Note: a: The solutions are obtained on the basis of finite element lower bound with the help of interior point method.
b: The solutions are obtained on the basis of limit theorems by using the Optum G2 software. The values within and outside the parenthesis indicate the upper and lower bound solutions, respectively.
c: The solutions are obtained by centrifuge test
d: The solutions are obtained by limit equilibrium method

and Ghosh (2005) and Keshavarz and Kumar (2017) based on slip line solution, and (iii) Benmebarek et al. (2012) with the aid of finite difference code, FLAC. The lower bound solutions of Kumar and Chakraborty (2015) were obtained by linearizing the Mohr-Coulomb yield criterion; whereas, the solutions by Tang and Phoon (2018) were from

Optum G2 software based on second order cone programming. The present N_γ values are almost similar to the results provided by Tang and Phoon (2018). However, the stress characteristics solutions, especially the solutions provided by Kumar and Ghosh (2005), and the finite difference solutions are appreciably higher than the present solutions.

Table 4.8. A comparison of N_γ values for ring footing on sand layer with ϕ equals to 20°, 25°, 30°, 40°, and r_i/r_0 equals to 0.25, 0.5, 0.75.

ϕ	r_i/r_0	Present Work[a]	Tang and Phoon (2018)[b]	Keshavarz and Kumar (2017)[c]	Kumar and Chakraborty (2015)[d]	Benmebarek et al. (2012)[e]	Kumar and Ghosh (2005)[c]
20°	0.25	1.888	1.81	1.87	1.84	2.33	2.36
	0.5	1.642	1.56	1.64	1.85	2.18	2.74
	0.75	1.6	1.41	1.51	2.32	2.4	3.12
25°	0.25	4.78	4.71	4.93	4.68	6.15	5.87
	0.5	3.864	3.83	4.08	4.22	5.36	6.94
	0.75	3.568	3.37	3.56	5.2	5.68	8.16
30°	0.25	12.72	12.8	13.4	12.4	17.2	15.6
	0.5	9.51	9.64	10	9.76	13.9	18.4
	0.75	8.17	7.99	8.44	10.1	13.7	21.4
40°	0.25	122.81	127	136	131	177	139
	0.5	75.14	79.5	83.5	103	132	171
	0.75	50.76	53.5	67	81	39.1	207

Note: a: The solutions are obtained on the basis of finite element lower bound with the help of interior point method by smoothening the yield criterion.
b: The solutions are obtained on the basis of limit theorems by using the Optum G2 software.
c: The solutions are based on slip line solutions
d: The solutions are obtained on the basis of finite element lower bound after linearizing the yield criterion.
e: The solutions are obtained on the basis of FDM code, FLAC.

Table 4.9 further presents a comparison between the present N_γ values with the experimental solution of Saha (1978) by choosing two angles of dilation, namely, $\psi = \phi$ and $\psi = \phi/2$. Following the work of Drescher and Detournay (1993), an equivalent friction angle (ϕ^*) was computed for the chosen dilatancy angle. It was observed that

for larger annular section of the foundation, the experimental solution of Saha (1978), especially for the higher friction angle (ϕ > 35.5°), is in good agreement to the solution that was obtained by taking $\psi = \phi/2$. This comparison clearly reveals that the present bearing capacity factors are overpredicted due to the consideration of excessive dilation, and therefore the nonassociated flow rule is required to employ realistic solutions.

Table 4.9. Comparison of N_γ values for ring footing on homogenous sand

ϕ	ϕ*	r_i/r_0	Present study		Saha (1978)
			$\psi=\phi/2$	$\psi=\phi$	
31°	29.92°	0.2	13.47	16.88	13.79
		0.4	10.33	12.75	13.37
		0.6	8.63	10.64	14.75
35.5°	33.9°	0.2	31.61	45.2	45.33
		0.4	23.03	31.85	36.3
		0.6	18.1	24.61	35.2
38.68°	36.63°	0.2	66.41	96.04	66.8
		0.4	47.23	65.98	63.82
		0.6	36.04	47.4	51.42
40.5°	38.17°	0.2	96.88	152.75	89.05
		0.4	68.52	102.67	67.28
		0.6	50.24	69.33	71.18

Source: Data from Saha (1978).
a: The solutions are obtained based on finite-element lower bound with the help of IPM by smoothening the yield criterion.
b: The solutions are obtained from the laboratory experiment.

4.7 SUMMARY

The advantages of placing sand over clays in improving the ultimate bearing capacity of ring footing are rigorously investigated with the usage of lower bound limit theorems in conjunction with finite elements and nonlinear optimization. The lower bound analysis is carried out by smoothening the yield criterion. The benefits of the inclusion of the sand layer are reported in terms of a non-dimensional efficiency factor. The values of efficiency factor are thoroughly examined by extensively varying the

strength of the layers, size of the annular section, thickness of the sand inclusion, and soil-footing interface conditions. The efficiency factor increases with increase in the surcharge pressure, footing roughness, strength and the thickness of the sand layers. An optimum thickness of the sand layer appears to exist distinctly for each case beyond which no further strength improvement is noticeable. The magnitude of optimum thickness increases with increase in ϕ, and $q/(\gamma r_0)$, but decreases with increase in the value of r_i/r_0 and $c_u/(\gamma r_0)$. A specific radius ratio also appears in most of the cases for which the efficiency factor is maximum. The failure pattern indicating the plastic zone within the soil is drawn for few cases which reinforces the numerical observations. The results are compared with available results from literature and found to be quite satisfactory.